

POLITECNICO DI TORINO

Master's Degree in
NANOTECHNOLOGIES FOR ICTs

Master Thesis
Production and Characterization of Electrospun Carbon
Nanofibers as Cathode Support for Sodium-Ion Cells



First Advisor: Prof. Claudio Gerbaldi
Second Advisor: Prof. Carlo Ricciardi

Candidate:
Lorenzo Lucherini

Supervisor: Prof. Jürgen Brugger

Academic Year 2018-2019

Contents

Acknowledgments	ii
Abstract	iii
1 Background and Motivations	1
1.1 Batteries Fundamentals	1
1.2 Lithium-Ion and Sodium-Ion Batteries: Technology and Perspectives	4
1.3 Electrospinning	8
1.4 Electrospun CNF for Battery Electrodes: State of the Art	13
1.5 Purpose of the Work	14
References	15
2 Materials and Methods	19
2.1 Electrospinning and Production of CNF	19
2.2 Characterization Techniques	21
References	24
3 Results and Discussion	26
3.1 Fibers and Mats: Morphology after Spinning, Stabilization and Carbonization . .	26
3.2 Dependence of Mat Thickness on Volume of Spun Solution	27
3.3 Assessment of Stabilization via FTIR	29
3.4 Carbonization and its Effects on CNF Structure and Conductivity	30
References	33
4 Conclusions and Outlook	35
References	36
5 APPENDIX	37

Acknowledgments

I would like to acknowledge Prof. Jürgen Brugger and Prof. Giovanni Boero for supervising and supporting this project. Despite its being slightly off-topic with respect to the laboratory research line, all the valuable discussions and feedbacks highlighted their commitment and curiosity for every aspects of science and engineering.

Prof. Claudio Gerbaldi for supervising this work from the other side of the Alps and reviewing this document. His team members, Dra. Meligrana and Drs. Colò for helping with the electrochemical characterizations.

My friend and project mate Jacopo Celè for proposing and developing this project side by side. For being a brilliant scientist and engineer and shedding light on the pleasures of automation and coding.

Prof. Doretta Capsoni and Dr. Irene Quinzeni for introducing fundamental theoretical and experimental aspects of battery physics and manufacturing.

Prof. Van Herle of EPFL Group of Energy Materials and his friend and colleague Prof Hugh Middleton of Agder University for the interesting discussions about the future of energy storage.

Prof. Mario Paolone for his engineering perspectives on stationary energy storage.

I would like to thank Lorenz Hagelüken for the usage of glove box and tube furnace and all the members of LMIS1 for their help and for becoming good friends during these six months. For talking about science and life in the cosy room.

A special thanks is dedicated to the Lausannois: Giulia, Gloria, Jacopo, Costantino Marco and Alessio, for being my family in Lausanne.

To Petro and Teo, my other two traveling mates, whose friendship overcomes every time zones.

To my brother, to my mother and to my father for their invaluable support.

Abstract

Sodium-ion batteries (SIB) are promising alternatives to lithium-ion batteries (LIB) thanks to their cost effectiveness deriving from the usage of low cost, widely abundant precursors. The absence of rare elements like cobalt, now employed in the majority of LIB, is a decisive features which could push battery manufacturers to consider SIB as a viable parallel technology to LIB. Although suffering from lower gravimetric and volumetric energy and power densities with respect to LIB counterparts, SIB could play a decisive role in fostering the transition to renewables sources by providing low cost batteries capable of storing energy generated by solar and wind power. Concerns about batteries weight and volume are of second order when dealing with stationary storage, thus SIB could compete with LIB mainly thanks to the possibility of a large and low cost mass production.

Well established battery companies like SAFT® forecast the launch of SIB on the market in three to four years time¹. Meanwhile, more than 7000 papers have been published in the last five years², highlighting the interest and effort in designing, synthesizing and engineering materials for SIB.

The present work was part of a broader project proposed and planned by Jacopo Celè and myself and conducted in the laboratory LMIS of EPFL under the supervision of Prof. Jürgen Brugger (EPFL) and Prof. Claudio Gerbaldi (Politecnico di Torino).

The final aim was the production of a sodium-ion cell based on $\text{Na}_2\text{V}_3(\text{PO}_4)_3$ (NVP), one of the most studied and promising cathode materials for SIB. Yet, NVP has low electronic conductivity, resulting in poor performances, especially when high currents need to be drawn from the cell. One way to enhance electrical conductivity is by exploiting a conductive and porous matrix which supports NVP particles and reduce the internal resistance, boosting the performances of the battery. This type of structure is usually called electrode support.

On these basis, the project was split into two parts. The first was concerned with the production and characterization of the conductive support by a low cost and scalable technique: electrospinning. Polymeric fibers down to tens of nanometers of diameter can be produced with this technique. In the most simple setup, fibers are arranged randomly on the plane, forming a non woven texture, similar to those obtainable in textile industry. Thick layers of stacked fibers, resembling a tissue mat, can be produced. In particular, carbon nanofibers can be obtained by pyrolyzing the mat. Carbon nanofibers mat have good electronic conductivity and porosity given by the non woven texture. They are thus ideal to be used as electrode support.

The second part was concerned with the assessment of different procedures to load the active material inside the support. Eventually, the CNF/NVP system was used as cathode in a sodium-ion cell and electrochemically characterized.

The present work reports the results of the first part. CNF were successfully produced and section morphology showed the presence of uniformly distributed and interconnected pores. Different mat thicknesses were obtained, from 20 μm to 1 mm. The role of support thickness is important since a thicker support can host more active material, thus increasing the cell energy content. Yet, electrolyte diffusion must be allowed by a highly porous structure.

¹[SAFT-Three battery technologies that could power the future](#)

²[Clarivate Analytics: Sodium Ion Battery Publications Report](#), accessed on 30/08/2019.

XRD, TEM and Raman spectroscopy indicated that CNF structure underwent partial graphitization upon carbonization. Electrical conductivity through the mat plane was about 10 mS cm^{-1} , lower than other reported value for similar procedures. Increase and optimization of electrical conductivity is therefore needed as future work.

The second part of the project is dealt with in J.Celè's thesis³.

³Jacopo Celè. "Study of the Effect of Carbon Nanofibers Electrodes Morphology on Sodium-ion Cells Electrochemical Performances". MA thesis. Politecnico di Torino, 2019

Chapter 1

Background and Motivations

The first section 1.1 introduces basic notions about batteries, the functioning principles and characteristic quantities. Some details about the kinetics of the discharge/charge process are highlighted, in order to provide a qualitative physical understanding of the motivations behind the proposed work. Section 1.2 present lithium-ion batteries and their competitive alternative, sodium-ion batteries, the rocking-chair working principle, the standard *slurry* based manufacturing process and how it affects battery performances. A few solutions to overcome limitations in slurry based electrodes are discussed and they contribute strongly to motivation underlying the experimental part.

Then, Section 1.3 describes the technique of electrospinning, a cost effective and scalable way to produce nanofibers of different materials. The process to obtain carbon nanofibers (CNF) with electrospinning is detailed and leads to Section 1.4, a state of the art review of electrospun CNF for battery applications.

To conclude with, Section 1.5 states the purpose of this work in the frame of the broader project carried out with J.Celè.

1.1 Batteries Fundamentals

What is a Battery: Some Definitions

A battery is a system capable of converting energy released by spontaneous chemical reactions into electricity. Such a conversion takes place in a fundamental unit, called cell. Each cell has three major components: a positive electrode (cathode), a negative electrode (anode) and an electrolyte (Figure 1.1a).

The cathode and the anode are the sites where chemical reactions happens in the form of an oxidation reduction reaction (redox), involving electron transfer to and from a couple of electroactive materials, called cathode active material and anode active material. The electron flow can be forced through an external circuit by physically separating the two electrodes. Internally, the circuit is closed by the electrolyte, a good ionic conductor in liquid or solid state. In real cells, anode and cathode are kept apart by a porous dielectric separator, permeable to a liquid electrolyte. Two metallic plates are used as conductive supports for the active materials and serve as current collectors (Figure 1.1b) The electrochemical process can be reversed in certain batteries where the recovery of the chemical composition of the active materials is possible upon electric energy intake. Such systems are referred to as secondary or rechargeable batteries, while non rechargeable devices are called primary batteries [1].

Basic Working Principles

Redox reactions are at the basis of cell functioning. They involve the net transfer of electrons between two chemical species, contained in the anode and cathode active materials.

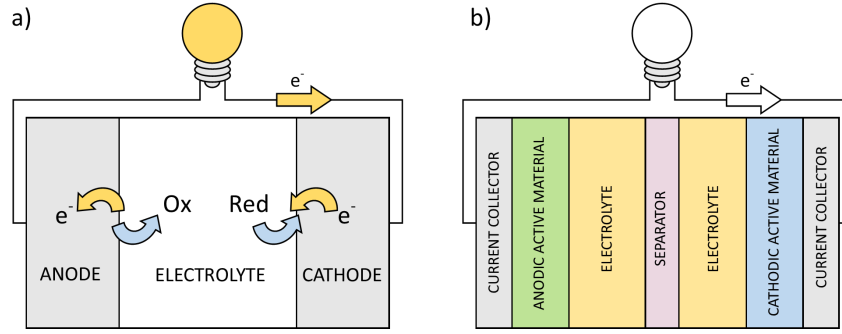
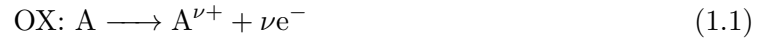


Figure 1.1: General schematic of a) cell main components and operation under discharge, b) main components of a real cell.

Redox reactions can be split in two half reactions in which electrons are released upon oxidation of species A and gained upon reduction of species B. Reactant A is said to be oxidized and its oxidation number increases. Reactant B is said to be reduced and its oxidation number decreases. The two half reactions are thus represented as follows (ν is the number of electrons involved in the reaction):



Overall, the reaction reads:



The two couples $A/A^{\nu+}$ and $B/B^{\nu+}$ are called redox couples. Each couple is characterized by a standard redox potential, whose value is a measure of the work needed to transfer one electron from the electrode to the redox couple in the electrolyte [2], under the standard condition of atmospheric pressure and 1 mol/L concentration of the liquid electrolyte. Similarly to electric potentials, they are measured with respect to a standard reference, commonly the standard hydrogen electrode (SHE) whose value is set to 0 V. It is common use to express such potentials with the notation:

$$[E_{\text{ox/red}}^{\circ}]_{\text{SHE}} \quad (1.4)$$

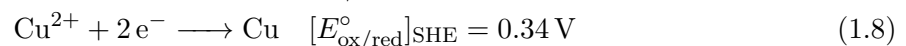
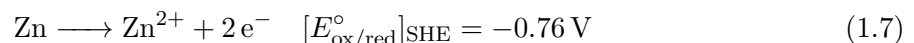
where the symbol $^{\circ}$ denotes the standard condition, ox/red indicates the given redox couple and SHE recalls the type of reference electrode used.

From standard redox potentials one can compute the standard potential of a cell, E_{cell}° , by means of:

$$E_{\text{cell}}^{\circ} = [E_{\text{cat}}^{\circ}]_{\text{SHE}} - [E_{\text{an}}^{\circ}]_{\text{SHE}} \quad (1.5)$$

where subscripts cat and an refers to the redox couples involved at the positive and negative electrode, respectively.

As an example, let us consider the redox reaction involved in a Daniel cell, a system composed of a zinc anode and a copper cathode, immersed in zinc and copper sulfate electrolytes, respectively. The overall process during discharge is represented by [2]:



At the anode, zinc undergoes oxidation from Zn^0 to Zn^{2+} , releasing two electrons. At the cathode, copper is reduced from Cu^{2+} to Cu^0 upon acquisition of two electrons. If the two reactions are physically separated, the system can reach the equilibrium by letting electrons flow from the anode to the cathode through an electrical circuit connecting the two electrodes. Such a current will flow under a cell standard potential of $E_{\text{cell}}^{\circ} = 1.10 \text{ V}$.

Characteristic Quantities

Several quantities are used to characterize a battery [3]. Hereunder, a short summary of the main quantities of interest for this work is reported.

Theoretical capacity The theoretical capacity (Q_t) of an active material is the maximum amount of charge that can be extracted. It is computed as [3]:

$$Q_t = zFM \quad (1.9)$$

where z is the number of electrons exchanged during the redox reaction, F is the Faraday constant ($96\,500\text{ C mol}^{-1} = 26\,800\text{ mAh/mol}$) and M is the molar mass of the active material.

Capacity and capacity density The capacity (Q) of a real battery system is defined as follows and expressed in Ah:

$$Q = \int_0^t I(t)dt \quad (1.10)$$

Capacity density is defined as the capacity per unit mass (Ah/g) or volume (Ah/L). Specific capacity per unit mass of active material is usually used in literature to compare different active materials in different cell setups.

C rate The C rate is a conventional way of representing the current used to charge or discharge a battery. A C rate of 1C discharges completely the battery in 1 h, 2C and C/2 discharge in 1/2 h and 2 h, respectively.

Nominal Capacity The nominal or rated capacity specified by a battery manufacturer is the capacity measured under standard condition of constant current discharge and room temperature. For example, a commercially available Li-ion storage system with nominal capacity of about 170 Ah at C/5 is fully discharge in 12 min if a 170 A current is drained.

Energy and energy density The energy (E) stored in a battery is expressed in Wh and can be related to the capacity by means of:

$$E = Q \cdot \bar{V} \quad (1.11)$$

where \bar{V} is the average discharge voltage. Energy density is the energy normalized on the mass of active material used (Wh/g) or on its volume (Wh/L).

Open circuit voltage The open circuit voltage (V_{OC}) is the voltage at the battery terminals when no load is applied:

$$V_{OC} = -\frac{1}{nF}(\mu_a - \mu_c) \quad (1.12)$$

where μ_a and μ_c are the electrochemical potential of the anode and the cathode, respectively. It is equivalent to Equation 1.5.

Cycle life The cycle life for a rechargeable battery is the number of charge/discharge cycles performed before the capacity fails to a point of fixed capacity (usually 80%).

Charge efficiency Charge efficiency (or Coulombic efficiency, CE) is the ratio between capacity during discharge and capacity during charge, expressed as a percentage. High CE means that the battery has a highly reversible charge/discharge process and almost all the energy provided during charge can be supplied back during discharge.

Elements of Battery Kinetics

The charge and discharge process of a battery is determined by many kinetic parameters which deeply affect its performances.

When an external circuit is connected and a current is drained, redox reactions at the electrodes must happen at a rate capable of sustaining the current requested by the user. This is only partially given by the reaction rate itself. The overall kinetics of a functioning battery can be split in several steps (Figure 1.2) [4, 5]:

- *Ions transport through the electrolyte.* Cations and anions must move through the electrolyte to reach the active material. Two main mechanisms determine ionic transport: diffusion, due to the electrolyte concentration gradient between the bulk electrolyte and the electrolyte-active material interface, and electric migration, caused by the electrode potential on charged species. This step can be modeled by an equivalent ionic resistance R_{el} .
- *Ions diffusion inside the active material.* This step is peculiar of lithium and sodium-ions systems, where Li^+ is reduced upon intercalation between crystal planes of active material. In this case, the ion has to diffuse inside the active material particle and therefore the process is described by a solid diffusion constant D_s [4].
- *Electric charge transfer* After the redox reaction, the generated electron is still inside the active material particle. A potential barrier imposed by the particle surface is to be overcome to extract the electron and drain it towards the current collector to contribute to the generated current. This process can be modeled in terms of a charge transfer resistance R_{ct} [6].

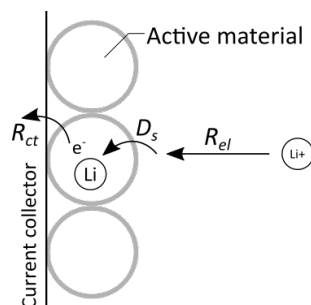


Figure 1.2: Schematic of the steps involved during the discharge of a battery.

An electrode suffering from high R_{el} , R_{ct} and low diffusivity in the solid state exhibits poor performances in terms of C rate: the outer circuit requires many electrons to be generated but ion diffusion is too slow to provide enough species for the redox reaction. Moreover, a high R_{ct} affects the electrode capacity since electrons struggle to find low resistance path to leave the active material and reach the collector. Thus, very few charges can be exploited and the cell capacity drops below Q_t .

1.2 Lithium-Ion and Sodium-Ion Batteries: Technology and Perspectives

Some of the most widely used types of secondary batteries are shown in Figure 1.3a. They all exploits different active materials and electrolytes, for instance the nickel-cadmium (Ni-Cd), commonly used in portable electronics, is composed of a NiOOH cathode, Cd anode and uses an

alkaline electrolyte, KOH. Lithium-ion batteries (LIB) relies on a slightly different functioning mechanism with respect to the other systems. A typical LIB is composed by a LiCoO_2 (LCO) cathode, a graphite anode and an electrolyte made of LiPF_6 dissolved in a mixture of ethylene carbonate and propylene carbonate (EC/PC). During discharge, thanks to the layered structures of the electrode materials, Li^+ undergo a process of deinsertion, or *deintercalation*, from the graphite planes and moves towards the cathode, where it *intercalates* within the crystal planes of LiCoO_2 . Intercalation and deintercalation are supported by the following redox reaction:



yielding $E_{\text{cell}}^{\circ} = 3.70 \text{ V}$.

During charge, Li^+ shuttles back, deintercalating from the cathode and intercalating in the graphite planes. This ion shuttling mechanism, back and forth, is also called *rocking chair* (Figure 1.3b). The choice of using graphite anode arose from safety reasons linked with the

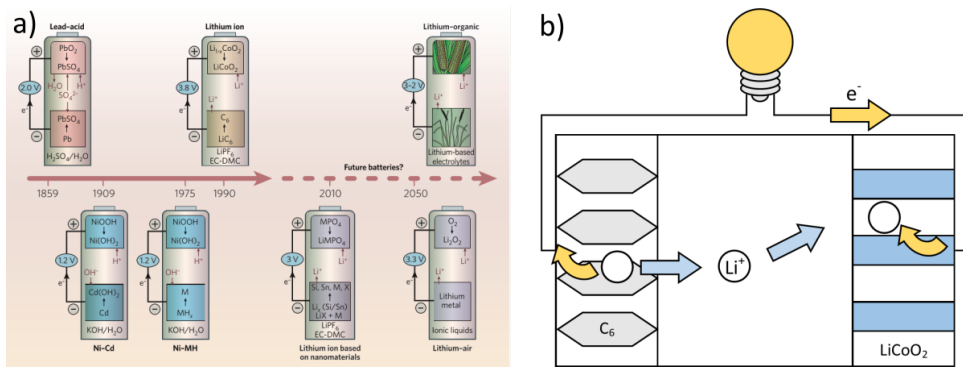


Figure 1.3: a) Types of secondary batteries and their chemistry. Taken from [7]. b) Schematic representation of rocking chair principle in a discharging LIB.

previous use of metallic Li as negative electrode. Graphite theoretical capacity (372 mA h g^{-1}) is ten times lower than metallic Li (3860 mA h g^{-1}) but advantages in terms of safety and cost outbalanced the loss of capacity, making graphite the first choice in terms of LIB anodes.

On the cathode side, several Li compounds are used by manufacturer, mostly LiMn_2O_4 (LMO), LiNiMnCoO_2 (NMC) and LiFePO_4 (LFP) and electrodes are all produced with the same process flow (analogous for anodes) [8]:

1. *Slurry preparation.* Active material in the form of powder is mixed together with a conductive filler, like carbon black or graphite, and a PVDF binder. Conductive filler helps enhancing electronic conduction, very low for active materials such as Li oxides. Binder is needed to keep the mixture together but, being a polymer of low electrical conductivity, it works partially against the good performance of a cell. The mixture is dissolved in a solvent so that a dense paste, *slurry*, is made.
2. *Doctor blade coating.* The slurry is poured on aluminum or copper foil, the current collectors, and coated on the surface by doctor blade technique. The thickness of the final coating is controlled by the height of the blade and it usually ranges between $30 \mu\text{m}$ and $50 \mu\text{m}$ for commercial cells.
3. *Calendering.* The paste-collector system is calendered in a roll-to-roll process. Pressure and heat creates a uniform film of active material on the collector surface. The electrode is then punched or cut and used to assemble the cell.

One of the most important features of the *slurry-based* process is the simplicity with which cell energy, or power, can be adjusted. Roughly speaking, if one is to maximize the energy content,

the parameter to tune is the active material concentration in the slurry. Instead, to achieve high power performances, *i.e.* high C rate, thin electrodes are produced, reducing the path needed to extract electrons.

From this simple description, a fundamental properties of batteries exploiting slurry-based electrodes can be understood: energy and power cannot be maximized at the same time. A trade off between thick, high energetic electrodes and thin, high power electrodes is always necessary [9]. The effects of thick electrodes, its limitations and possible ways to overcome them are open fields of research [9, 10, 11].

Enhancing Battery Performance: Porous Electrodes and Electrodes Support

A way to improve battery performance is by acting on the kinetic parameters. The most widely investigated approach, both at research and manufacturing level, is the use of porous electrodes. These benefits of these structures were formalized in the seminal works by J. Newman [12, 13] and can be summarized as follows:

- *Reduced ion diffusion path.* A porous electrode allows electrolyte to diffuse easily and effectively throughout the whole electrode thickness. Reaction kinetics dependence on electrolyte diffusion is thus lowered.
- *Reduced ohmic drop.* In a slurry-based electrode, electrons can be generated only at the interface between electrolyte and the surface of the slurry coating (*reaction zone* [13]). This means that electrons see the whole electrode thickness as a resistive path which increases the internal resistance of the cell. If the electrolyte is uniformly distributed, electrons can be generated closer to the current collector, seeing a lower resistive path.
- *Active material utilization.* A higher amount of active material is reached if electrolyte can diffuse through the electrode. This is particularly significant in the case of thick electrodes, where one wants to exploit the whole active material and not being limited by the thickness itself.
- *Mechanical stress absorber.* Materials for rocking chair electrodes have to withstand severe mechanical stress of the crystalline structure each time that the shuttling ion intercalates/deintercalates. After a high number of cycle, such process may cause the collapse of the structure and the delamination of the slurry from the current collector. Pores can support this cyclic stress by providing void space for the active material to expand and contract.

A qualitative schematic of slurry and porous electrode is shown in Figure 1.4. Advantages of porous structures are often combined with electrodes *support*, namely electrically conductive networks of interconnected pores that offer structural support to the active material allowing at the same time good electrolyte diffusion and good electrical conductivity.

Alternatives to Lithium: Sodium

Quite surprisingly, when at the beginning of 1980 J. Goodenough proposed LCO and similar Li oxides now commonly used in commercial LIB, another class of material based on sodium compounds was under research by the same group [14]. Na-based compounds like $\text{Na}_3\text{M}_2(\text{PO}_4)_3$, M being a transition metal such as Zr, V, Cr, Fe and Ti, were called Na Super Ionic Conductor (NASICON) thanks to their high solid ionic conductivity. The interest in this family of active materials was however partially overshadowed by the commercialization of the first LIB by Sony in 1991 based on LCO and graphite, event that drove the attention almost entirely on development of LIB materials.

Then, in the last ten years, sodium-based materials for sodium ion batteries (SIB) as an

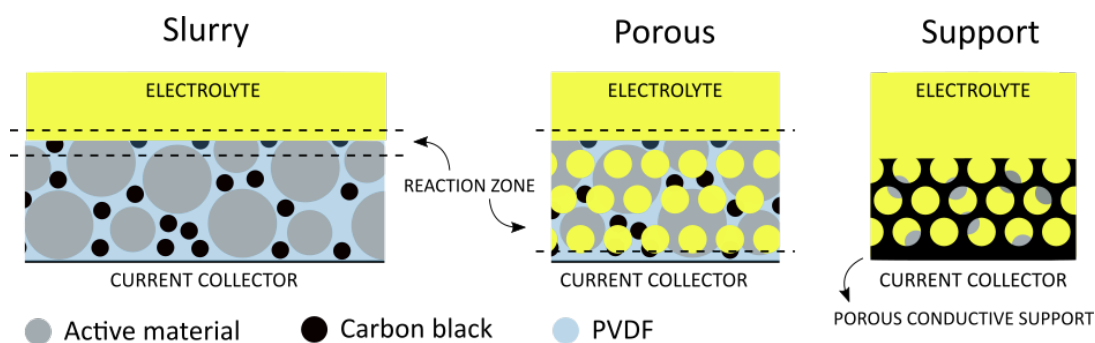


Figure 1.4: Schematic diagrams of a standard slurry based and a porous electrode. Porosity enhance diffusion of the electrolyte throughout the thickness, allowing better utilization of active material and shorter electron transfer path to the collector.

alternative to LIB has proven to be a very hot topic both for fundamental research [14, 15] as well as for well established battery manufacturer [16]. The reason behind this renovated interest is the need to develop cost effective and environmentally compatible alternatives to LIB to be exploited mainly in the field of stationary energy storage, promoting the integration of renewable sources in the grid.

Compared to LIB, SIB precursors are cheaper and abundant [17]: battery grade Na_2CO_3 is 10 times cheaper than the equivalent Li_2CO_3 and Na is 100 times more abundant than Li in mining composition. Moreover, Co is the real bottleneck for LIB production being one of the less abundant materials on Earth crust and being almost entirely used by battery industry (more than 80% of world extraction in 2018). On top of the beneficial effects of Na-Li exchange, SIB can use aluminum as current collectors for both electrodes, whereas LIB must use copper collector on the anode side due to the formation of Li-Al alloys at low potentials. This represent another economical factor to be considered as the replacement of Cu by Al accounts for more than half of the 4.3% reduction on the final battery cost arising from exchanging Na with Li and Cu with Al.

SIB work exactly with the same rocking-chair mechanism as LIB, yet physical differences between the two ions entails a few differences in the cell composition. The higher ionic radius of Na^+ (1.02 Å versus 0.76 Å of Li^+) makes intercalation in graphite anodes not efficient. Graphite must be substituted by amorphous structures with inter planes defects where Na^+ can be stored. In terms of cathode active material, the following families are the most promising for commercial SIB [18, 14]:

- *Layered Metal Oxides.* Compounds like NaMnO_2 or NaFeMnO_2 offer specific capacities up to 200 mA h g^{-1} and voltage of $\sim 3 \text{ V}$. The most remarkable feature is the cost, abundance and environmental compatibility of precursors. Yet, they are highly sensitive to moisture since the wide inter plane spacing can easily intercalate water molecules which form oxides on the material surface. They are also reported to suffer from poor cycle life due to lattice distortion during intercalation/deintercalation.
- *NASICON Polyanions.* $\text{Na}_3\text{V}_2(\text{PO}_4)_3$, $\text{Na}_3\text{Ti}_2(\text{PO}_4)_3$ and $\text{NaV}(\text{PO}_4)\text{F}$ are NASICON material with very high ionic conductivity ($> 1 \text{ mS}$), structural stability and specific capacities up to 180 mA h g^{-1} , able to work at voltages of $\sim 3.40 \text{ V}$, comparable to LIB. Remarkably, they can be used to assemble symmetric cells where both electrodes are composed of $\text{Na}_3\text{V}_2(\text{PO}_4)_3$, for example, thanks to the double redox couple $\text{V}^{3+}/\text{V}^{4+}$, $\text{V}^{2+}/\text{V}^{3+}$ [19]. As a drawback, the very low electronic conductivity forces the use of conductive fillers or cathode supports.

Figure 1.5 compares several cathode materials studied for SIB and currently used LIB materials. In general, performances in terms of energy and power of SIB are always inferior to those of

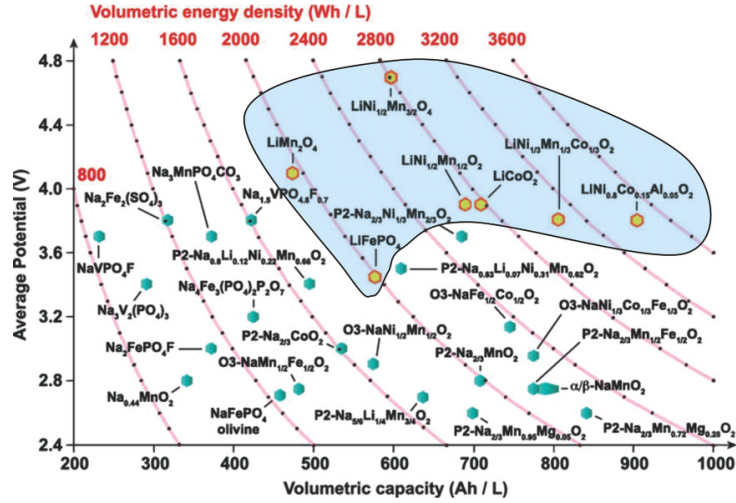


Figure 1.5: Comparison of materials for SIB and LIB in terms of output voltage, energy and capacity density. Taken from [14].

LIB due to fundamental differences in Na and Li ions and their electrochemistry. Thus, the real advantages of SIB can be reasonably circumscribed to their application in stationary energy storage, where battery mass and volume play secondary roles to with respect to battery cost [15, 14].

1.3 Electrospinning

Working Principles

Electrospinning is a versatile, scalable and cost effective technique to produce polymeric fibers having diameter ranging from few micrometers down to tens of nanometers.

Standard polymer manufacturing processes such as wet or melt spinning can only achieve fiber diameters higher than 1 μm and time consuming and expensive CVD methods have to be employed if nanofibers are to be produced.

Electrospinning has become a valid alternative and its efficiency and simplicity is based on the interaction between a liquid solution and an externally applied electric field.

The basic setup for electrospinning is composed by the following components: a high voltage source, a metallic needle (*spinneret*) and a grounded collector. The polymer solution is usually loaded in a syringe and supplied to the needle at a constant and controllable rate by a syringe pump. A high voltage, from 10 to 20 kV, is applied between the needle and the collector. The collector is commonly a metal plate placed either vertically or horizontally with respect to the needle (Figure 1.6).

A pendant droplet is formed at the tip of the spinneret when the solution is fed through (Figure 1.7a, original picture from this work). If the voltage is switched on, the electric field will induce charges on the droplet surface (Figure 1.7b). Two competing forces are present: surface tension, maintaining the droplet hemispherical shape and electrostatic repulsion among induced charges, deforming the droplet shape [20, 21, 22].

As the voltage is increased, electrostatic force starts overcoming surface tension, elongating the drop in a conical shape, the *Taylor cone* (Figure 1.7c). Further increasing the voltage over a threshold value causes the electrostatic force to overcome the liquid surface tension, resulting in the formation of a charged jet protruding from the cone (Figure 1.7d). The jet diameter close the Taylor cone apex is almost 100 μm and rapidly drops to about 10 μm in the first tenths of millimeters [20].

Once the jet is formed, a straight and stable filament can be observed. Diameter reduction

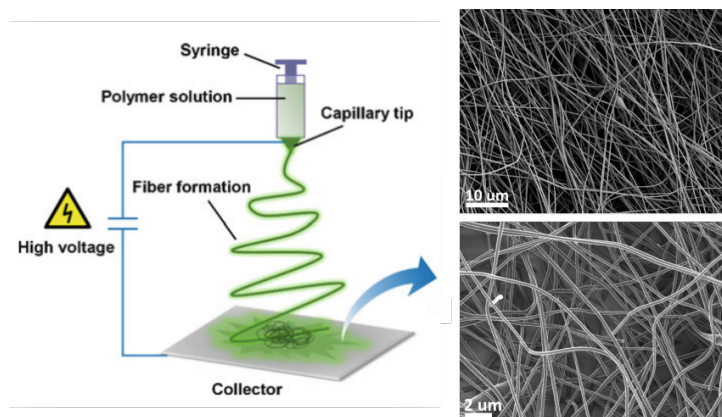


Figure 1.6: Schematic diagram showing basic setup components Adapted from [21]. On the right: example of spun fibers obtained in this work.

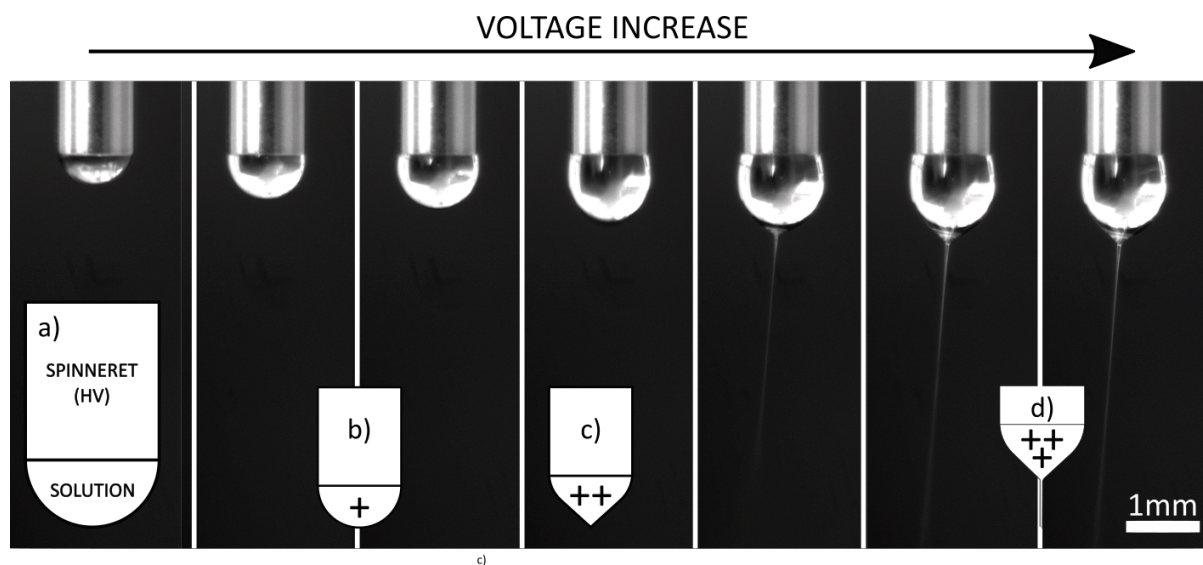


Figure 1.7: Real sequence of jet formation taken during the electrospinning process of this work with a digital camera. Schematic insets: a) pendant solution droplet; b) induction of charges on the surface; c) formation of the Taylor cone; d) jet emission and stretching. HV: High Voltage.

is due to the simultaneous action of jet stretching along its axis and solvent evaporation. A few millimeters away from the Taylor cone the evaporation of the solvent leads to an increase in charge density along the fiber, producing mutual repulsion among different sections of the filament. Under these circumstances, the jet experiences a *bending instability* [21], proceeding toward the collector in a looping and whipping manner.

Fibers are eventually deposited on the collector. The remaining solvent contained in the fibers evaporates and charges are neutralized through the grounded connection. If a simple plate collector is used, fibers are collected with random orientation, forming a layer characterized by non-woven texture as shown in Figure 1.6. As spinning progresses, layers of fibers are stacked one on top of the other, creating a sheet of variable thickness (*mat*).

Parameters

Despite its simplicity in terms of set up, many parameters determine fibers diameter and surface morphology. It is useful to sort these parameters in three categories: parameters of the solution, parameters of the process and parameters of the environment. A detailed description of these and other parameters can be found in [22, 21]. Hereunder, a brief overview of the main ones is reported for a clearer understanding of the following sections.

Solution parameters refer to the properties of the polymer solution used, therefore including its viscosity and surface tension.

- *Viscosity.* Solution viscosity (η) is determined by the polymer concentration and its molecular weight. Minimum value of η is needed to provide a stable jet. Below that value the droplet preferably splits into smaller droplets, producing an effect called electrospaying or electrostatic spray deposition (ESD) [23]. Thus, the higher η , the less effective the stretching and thicker fibers will be produced. Ellipsoidal or spherical swellings (*beads*) can be observed along the fiber axis if η is too low [22, 21].
- *Surface tension.* Being one of the two antagonistic forces in electrospinning, surface tension of the solvent used affects the intensity of the electric field required to form the jet. High surface tension solvents will require higher voltage than low surface tension ones.

Process parameters are related to the experimental set up and consist of applied voltage (V), needle to collector distance (d) and solution flow rate (Q).

- *Voltage.* The applied voltage, together with d , defines the electric field on the needle tip and hence the solution polarization. For a given experimental setup, d and Q being fixed, V has a certain voltage window within which the stability of the jet is maintained. The influence of V on the fiber diameter is negligible, even if opposite trends are also reported, revealing mainly a high dependence on the chosen polymer.
- *Tip to collector distance.* The distance between needle and collector (d) must be enough to let solvent evaporate before the fiber reaches the collector. For a given voltage, low d implies effective stretching but most of the solvent is still present, dissolving the collected fiber in an amorphous plastic film. For high d , solvent evaporation is almost complete but the reduced field may result in poor jet stretching. However, influence of d on the diameter is reported to play a secondary role [21].
- *Flow rate.* A suitable Q is the one balancing the solution removal rate so that a pendant drop is always present at the needle tip and the Taylor cone is stable throughout all the process. Increasing Q results in increasing the fiber diameter and faster mat deposition.

Ambient parameters include temperature and humidity of the setup environment.

- *Temperature.* Temperature affects indirectly the fiber diameter by altering the solution viscosity. A more direct effect is the increase of solvent evaporation rate which may cause clogging of the spinneret.
- *Humidity.* Humidity (relative humidity, RH) affects mainly the surface morphology of the fibers. Solvent evaporation is enhanced by a dry environment, thus low RH values foster the solidification of the fiber before landing on the collector. On the contrary, traces of solvent may still be present in the collected fibers at high RH, redissolving the polymer and losing the fiber shape [24]. Humidity influences the fiber surface for certain type of hygroscopic polymers [25] producing pores on the fiber surface.

Finally, it is worth mentioning that different fibers orientations are obtainable by changing the collector geometry. Aligned fibers can be collected by using two parallel grounded plates or rotating collectors. By changing the needles properties, for instance by using a coaxial spinneret, hollow fibers are producible.

The work of S. Ramakrishna [26, 27] can be referred to for extensive information on the effect of various collector geometries and needles.

Materials and Applications

Electrospinning has received growing attention in the last ten years thanks to its versatility in terms of processable materials. Nanofibers can be obtained from a wide range of polymers, both natural and synthetic, as well as from ceramic materials. The combination of both is also possible and rather simple by mixing polymer solutions with fillers, in particular ceramic or metallic nanoparticles, producing fibers with enhanced and tunable mechanical and chemical properties. This technique is often referred to as *co-spinning*.

Moreover, material characteristics are combined with peculiar features emerging from the single fiber morphology and, on a larger scale, from the layered complex of spun fibers. Together with the increased surface area typical of nanoscale objects, spun mats of disordered fibers exhibit a porous and interconnected structure inherent of non-woven textures.

Electrospun mats are thus of enormous interest for those applications where highly porous, interconnected and, if necessary, functionalized structures are highly desirable, such as in energy storage, environmental and biomedical fields.

In the following, a short review of environmental and biomedical application is presented [28, 29]. Applications to electrochemical energy storage are separately treated in Section 1.4.

Environmental Application Air and water filtration are two major applications of non woven mat thanks to their high porosity and high surface area which enable a higher number of interaction sites. They show effective removal of micrometer size air pollutants particles via physical trapping and adsorption on fibers surface and less pressure drop across the membrane. Removal of contaminants from water benefits from the interconnected network of fibers which allows good permeability and can be functionalized with ceramic oxides or hydroxides to enhance the filtration of heavy metal particles. Carbon-based fillers are often inserted to enhance the removal of organic compounds. In both cases, synthetic polymers such as polyamide (PA), polyvinyl alcohol (PVA) and polyurethane (PU) are widely exploited.

Biomedical Application Electrospun structures made of biocompatible and biodegradable materials are widely investigated in the field of tissue engineering as porous supports (*scaffolds*) to promote cell growth and tissue regeneration. Natural polymers such as polylactic acid (PLA), poly(lactic-co-glycolic acid) (PLGA), polycaprolactone (PCL), collagen, and silk are used in the form of non woven or aligned fibers. Fiber surface can be functionalized to provide cells nutrients and drugs and mechanical properties can be modified using fillers to adapt to the tissue environment and provide structural support during the regeneration process.

Production of Carbon Nanofibers (CNF)

Among the many types of fibers produced via electrospinning, carbon nanofibers (CNF) deserve special attention thanks to their high electrical conductivity, high Young's modulus and tensile strength.

In general, the production of CNF requires polymeric precursor fibers to undergo high temperature heat treatments in inert atmosphere. During such process, called pyrolysis or carbonization, non carbon atoms are removed, yielding fibers with carbon content up to 95% [30]. Frequently used polymers yielding high quality CNF are polyacrylonitrile (PAN), polyimide (PI), polyvinylidene fluoride (PVDF) and PVA but any other polymer having a carbon backbone could be exploited. The carbon structure composing the fiber show different degree of crystallization depending on carbonization temperature and process time, affecting directly the value of electrical conductivity which can reach 1000 S cm^{-1} for very high temperature process.

CNF possess also remarkable mechanical properties, having Young's modulus ranging from 50 to 200 GPa and tensile strength up to few GPa [31]. These properties are strongly dependant on the carbonization temperature.

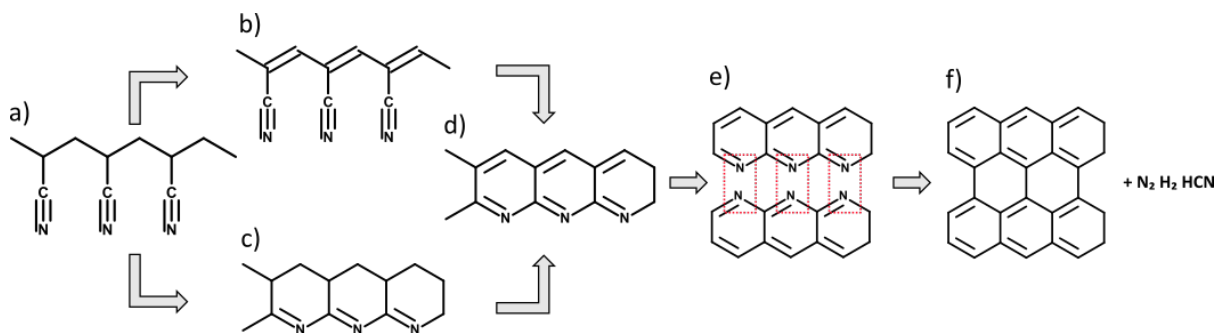


Figure 1.8: Chemistry of PAN stabilization and carbonization process.

CNF from PAN: Production Process Polyacrylonitrile has been the main choice for producing high quality carbon fibers since their first introduction in aerospace industry to produce high modulus and high strength composite materials. PAN has linear formula $(C_3H_3N)_n$, carbon contributes to more than half of the total molecular weight leading to CNF having more than 90% carbon content.

Precursor solution is usually composed by PAN dissolved in dimethylformamide (DMF) or dimethylacetamide (DMAc) in 5 to 10wt%. The mat is then processed with a first low temperature treatment (*stabilization*) followed by carbonization. Stabilization is fundamental to obtain fibers able to withstand high temperature pyrolysis. Without this intermediate step PAN would melt (melting point: 300 °C) or degrade, losing the fiber morphology.

Chemical processes behind stabilization and carbonization and their effects on the final CNF are detailed hereunder. For extensive information on PAN behavior during thermal stabilization one can refer to [30, 32, 33]. Optimization of process parameters and their effects on CNF properties are well explained in [34, 35].

Stabilization Stabilization is carried out right after the spinning process. PAN fibers are treated between 200 and 300 °C in air in order to promote the transformation of the linear PAN molecule (Figure 1.8a) into a structure having several parallel backbones connected together. This structure is known as *ladder* structure (Figure 1.8d) and provides polymer with high thermal stability.

Dehydration and cyclization are the two main chemical processes taking place during stabilization. Dehydration, *i.e.* hydrogen removal, occurs thanks to the oxygen rich atmosphere. Carbon is left with a free bond, which rearrange to form a C=C bond along the carbon chain (Figure 1.8b). During cyclization the triple bond C≡N is converted to C=N, allowing the formation of a ring structure (Figure 1.8c). Oxygen is not directly involved in the cyclization process, therefore this process can take place also in inert atmosphere. However, the presence of oxygen is reported to create highly active sites which enables the lateral linking of several ladder structures to form a graphite-like layer and therefore better CNF are obtained if stabilization is conducted in air.

Carbonization Carbonization is performed in inert atmosphere (nitrogen or argon) at temperature ranging from 800 to 1500 °C. In this step ladder structures are linked together thanks to the removal of nitrogen (Figure 1.8e) and remaining hydrogen. Nitrogen, hydrogen and other gaseous byproducts are released.

The resulting carbon sheets are arranged randomly with respect to the fiber axis, thus the CNF phase is usually amorphous. Orientation of carbon layers is possible by increasing the carbonization temperature up to 3000 °C, allowing the formation of a graphitic structure and CNF with electrical conductivity up to 1000 S cm⁻¹.

1.4 Electrospun CNF for Battery Electrodes: State of the Art

The structural and electrical properties of electrospun non woven CNF are features that well match the requirements of an ideal battery electrode: high electrical conductivity, to lower the internal resistance and porous interconnected structure, to allow electrolyte diffusion and complete utilization of the active material.

They currently represent a promising way to develop conductive supports for LIB and SIB anodes and cathodes, requiring no current collectors (*self-standing*). In particular, cathode active materials suffering from low electronic conductivity and low cycle life when used in slurry-based electrodes can achieve better performances in terms of higher C rate, longer life cycle and higher Coulombic efficiency if combined with a conductive support.

In the following, recent works dealing with electrospun CNF for supports and self-standing electrodes are summarized and compared. Table 1.1 present a comparison between performances of SIB materials when used in conventional slurry and in conjunction with CNF support.

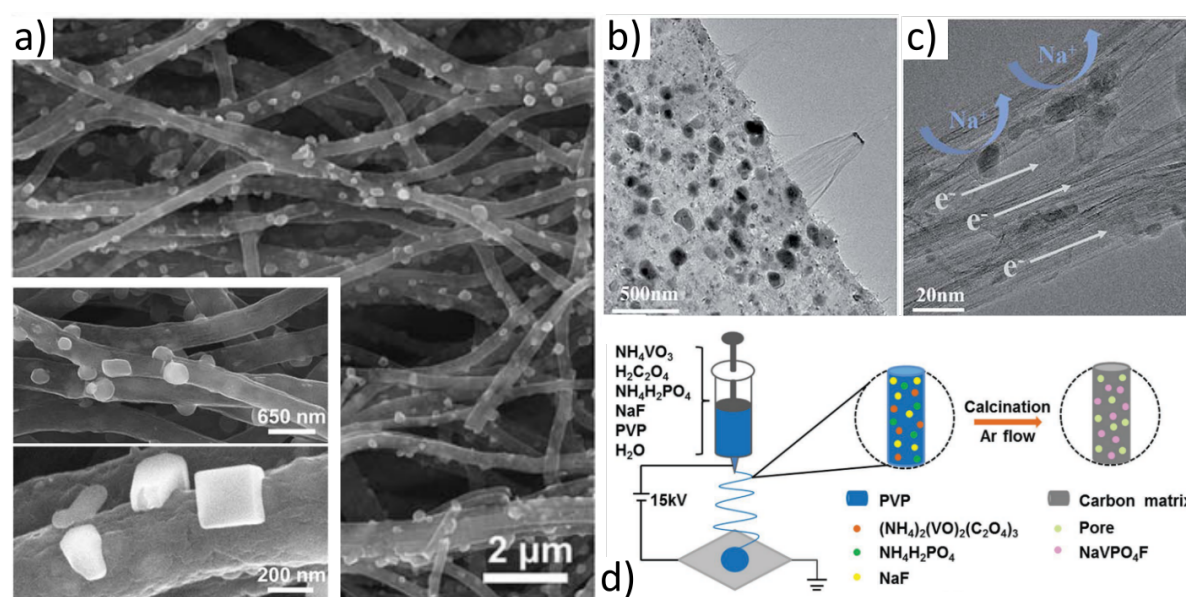


Figure 1.9: Examples of CNF as cathode support: a) LVP nanocubes grown on CNF surface via spinning of precursor solution and PAN (adapted from [36]); b) and c) NVP nanoparticles obtained by soaking of CNF in NVP precursor solution followed by annealing (adapted from [37]); d) widely used procedure to embed active material particles in CNF via co-spinning (adapted from [38]).

Self-standing anodes CNF sheet can be used as anodes for LIB and SIB without any further processing. Yu et al [39] suggested that Li ions intercalation in PAN-based CNF carbonized at low temperature benefits from the high number of defects sites created by nitrogen removal, resulting in a capacity of 550 mA h g^{-1} , much higher than standard graphite anodes (370 mA h g^{-1}). However, low conductivity causes a rapid loss of capacity when C rate is increased. On the contrary, CNF treated at high temperature have higher graphitization level, thus intercalation among graphene planes is the main contribution to the capacity. Higher electrical conductivity enables C rate up to 5C without major capacity loss.

The possibility of electrospinning carbon precursors together with active material is broadly used to insert high capacity materials, having low conductivity, inside CNF. For example, Fe_2O_3 was spun together with PAN to obtain nanoparticles embedded in CNF [40]. This structure was characterized by a capacity of 530 mA h g^{-1} (C/5) showing 98% Coulombic efficiency after 1000 cycles at 4C.

Flexibility of the CNF mat was exploited to produce a foldable LIB capable of performing 100 cycles upon bending [41]. However, only low C rate were reported. Interestingly however, the

Material	Slurry			CNF cathode support			Ref.
	Capacity (mAh/g)	Cycle life	CE (%)	Capacity (mAh/g)	Cycle life	CE (%)	
LVP	110 (0,1)	200 (5)	NA	140 (0,1)	1000 (5)	NA	[36]
NVP	114 (0,05)	100 (0,05)	97	103 (1)	1000 (2)	96	[44]-[38]
NVP	106 (0,2)	30 (2)	96	114 (0,05)	700 (1)	90	[42]-[37]

Table 1.1: Comparison between performances of slurry-based electrodes and self-standing CNF cathode support. Numbers in parenthesis are C rates at which quantities were measured. Reference are listed in the order: slurry-CNF cathode support. Electrochemical measurements were performed in half cells with Li or Na anode. Electrolyte was 1 mol NaClO₄, NaPF₆ or LiPF₆. NA: data not available from the paper.

addition of zinc acetate or other metal salts to the spinning solution is presented as an effective approach to promote PAN stabilization at lower temperature, yielding flexible CNF.

Self-standing cathodes CNF for cathodes are usually exploited by mixing precursors of the active materials with the spinning solution (Figure 1.9d). Resulting fibers have either active particles embedded inside or grown on the fiber surface. Remarkably, active materials with SIB with poor or average cycling performance when tested with slurry-based electrodes, are reported to have high increase in the cycle life, high Coulombic efficiency and good performances at high C rate. These features are all consequences of morphology of the cathode. The high porosity of CNF mat allows active material particles to undergo volume expansion/contraction during the intercalation/deintercalation process without losing electrical contact with the surrounding CNF. The high C rate is also explained by the good permeability of the electrolyte inside the pores.

An example of high cycle life of 1000 cycles at 2C with 96% efficiency is reported in [38] for NaVPO₄F particles embedded in CNF core. Particles of few nanometers reduce Na ion diffusion path inside the active material and the presence of pores on the fiber surface is claimed to provide excellent electrolyte diffusion.

Improved cycle life is reported also for Li₂V₃(PO₄)₃ (LVP). Similarly to NVP, LVP has low electrical conductivity and low cycle life when used in slurry-based electrodes. CNF with LVP nanocubes partially embedded in the fibers were obtained by mixing LVP precursors with PAN solution (Figure 1.9a) [36]. Thanks to the peculiar arrangement on the fiber surface, LVP is both exposed to the electrolyte and in physical contact with the CNF. These two features are claimed to be the cause of the enhanced cycle life above 1000 at 5C. A very interesting approach for loading active material inside the mat is suggested by [37]. Commercial CNF were soaked in a solution containing NVP precursors. Then, NVP particles grow inside the support and recover the crystalline phase upon annealing at high temperature in inert atmosphere (Figure 1.9b,c). Such system was used as cathode in SIB half cell, reaching 4000 cycles at 20C with 96% efficiency. Apart from the impressive performances, the proposed process is interesting because of the simplicity, low cost and scalability in tuning the amount of active material by adjusting the precursor solution concentration and soaking time. Electrospun active material-CNF composites were also used upon pulverization as conductive fillers to prepare slurry-based electrodes. No increase in life cycle and Coulombic efficiency of NVP were demonstrated [42, 43], confirming that CNF implies enhanced performances only when used as self-standing support for the active material.

1.5 Purpose of the Work

Sodium-ion batteries are valuable alternatives to LIB for future generation of stationary storage systems and will play a key role in fostering the transition to renewables and their integration

in the power grid. The benefits arising from using low cost and environmentally compatible precursors can balance the lower performance in terms of energy and power densities when compared to LIB.

As explained in the previous sections, porous electrodes and supports can be used as "technology boosters", lending the term from the microelectronics jargon, and performances of active materials can be highly enhanced by using these structures.

The project, conducted with J. Celè, aimed to develop a low cost and scalable process to fabricate and load cathode support with SIB active material and assess its effects on cell performances. The material chosen was NVP, due to its good electrochemical performances but poor electronic conductivity, which can possibly benefit from the synergy with a conductive porous support [37]. However, the independence of the proposed process on the choice of the material is to be stressed. The general concept behind the CNF support and loading procedure is not linked to any specific material and any other active compound, appropriately prepared, can possibly be processed in the same way.

The workflow was split into two sub processes. The first one, presented in the following chapters of this document, deals with the production of the CNF support itself. Electrospinning was chosen as a scalable and cost effective technique to produce CNF mats of various thicknesses. Morphological, structural and compositional characterizations were conducted on fibers and mats throughout all process steps.

The second part is concerned with the loading of active material inside the support starting from a liquid phase precursor solution and using different procedures. Electrochemical characterization was performed to understand the effects of different mat thicknesses and morphologies on a cell performances. This part is explained J. Celè thesis [45].

References

- [1] C. Julien and Z. Stoyanov. *Materials for Lithium-Ion Batteries*. Ed. by C. Julien and Z. Stoyanov. Dordrecht: Springer Netherlands, 2000. DOI: [10.1007/978-94-011-4333-2](https://doi.org/10.1007/978-94-011-4333-2).
- [2] H. H. Girault. *Analytical and Physical Electrochemistry*. EPFL Press, 2004.
- [3] Malgorzata K. Gulbinska. "Lithium-ion Cell Materials in Practice". In: *Lithium-ion Battery Materials and Engineering: Current Topics and Problems from the Manufacturing Perspective*. Ed. by Malgorzata K. Gulbinska. Springer, 2014. Chap. 1, pp. 4–5. DOI: [10.1007/978-1-4471-6548-4](https://doi.org/10.1007/978-1-4471-6548-4).
- [4] Fangming Jiang and Peng Peng. "Elucidating the Performance Limitations of Lithium-ion Batteries due to Species and Charge Transport through Five Characteristic Parameters". In: *Scientific Reports* 6.June (2016), pp. 1–18. DOI: [10.1038/srep32639](https://doi.org/10.1038/srep32639).
- [5] Myounggu Park et al. "A review of conduction phenomena in Li-ion batteries". In: *Journal of Power Sources* 195.24 (2010), pp. 7904–7929. DOI: [10.1016/j.jpowsour.2010.06.060](https://doi.org/10.1016/j.jpowsour.2010.06.060).
- [6] H.A. Kiehne. *Battery Technology Handbook*. Ed. by H.A. Kiehne. Marcel Dekker, Inc., 2003.
- [7] M Armand and J.-M. Tarascon. "Building better batteries". In: *Nature* 451.7179 (Feb. 2008), pp. 652–657. DOI: [10.1038/451652a](https://doi.org/10.1038/451652a).
- [8] R. M. Dell et al. *Understanding Batteries*. Ed. by RSC. RSC, 2001.
- [9] Zhijia Du et al. "Understanding limiting factors in thick electrode performance as applied to high energy density Li-ion batteries". In: *Journal of Applied Electrochemistry* 47.3 (2017), pp. 405–415. DOI: [10.1007/s10800-017-1047-4](https://doi.org/10.1007/s10800-017-1047-4).
- [10] Gui Fu Yang, Kyung Yup Song, and Seung Ki Joo. "Ultra-thick Li-ion battery electrodes using different cell size of metal foam current collectors". In: *RSC Advances* 5.22 (2015), pp. 16702–16706. DOI: [10.1039/c4ra14485f](https://doi.org/10.1039/c4ra14485f).

- [11] Honghe Zheng et al. “A comprehensive understanding of electrode thickness effects on the electrochemical performances of Li-ion battery cathodes”. In: *Electrochimica Acta* 71 (June 2012), pp. 258–265. DOI: [10.1016/j.electacta.2012.03.161](https://doi.org/10.1016/j.electacta.2012.03.161).
- [12] John Newman and William Tiedemann. “Porous-electrode theory with battery applications”. In: *AIChE Journal* 21.1 (1975), pp. 25–41. DOI: [10.1002/aic.690210103](https://doi.org/10.1002/aic.690210103).
- [13] John Newman. “Optimization of Porosity and Thickness of a Battery Electrode by Means of a Reaction-Zone Model”. In: *Journal of The Electrochemical Society* 142.1 (1995), p. 97. DOI: [10.1149/1.2043956](https://doi.org/10.1149/1.2043956).
- [14] Claude Delmas. “Sodium and Sodium-Ion Batteries: 50 Years of Research”. In: *Advanced Energy Materials* 8.17 (2018), pp. 1–9. DOI: [10.1002/aenm.201703137](https://doi.org/10.1002/aenm.201703137).
- [15] Kudakwashe Chayambuka et al. “Sodium-Ion Battery Materials and Electrochemical Properties Reviewed”. In: *Advanced Energy Materials* 8.16 (2018), pp. 1–49. DOI: [10.1002/aenm.201800079](https://doi.org/10.1002/aenm.201800079).
- [16] Patrick Bernard. *Three battery technologies that could power the future*. 2019.
- [17] Christoph Vaalma et al. “A cost and resource analysis of sodium-ion batteries”. In: *Nature perspectives* (2018). DOI: [10.1038/natrevmats.2018.13](https://doi.org/10.1038/natrevmats.2018.13).
- [18] Xiangjun Pu et al. “Recent Progress in Rechargeable Sodium-Ion Batteries: toward High-Power Applications”. In: *Small* 0.0 (2019), p. 1805427. DOI: [10.1002/smll.201805427](https://doi.org/10.1002/smll.201805427).
- [19] Qiong Zheng et al. “Progress and prospect for NASICON-type Na₃V₂(PO₄)₃ for electrochemical energy storage”. In: *Journal of Energy Chemistry* 27.6 (2018), pp. 1597–1617. DOI: [10.1016/j.jechem.2018.05.001](https://doi.org/10.1016/j.jechem.2018.05.001).
- [20] Jayesh Doshi and Darrell H Reneker. “Electrospinning process and applications of electrospun fibers”. In: *Journal of Electrostatics* 35.2-3 (Aug. 1995), pp. 151–160. DOI: [10.1016/0304-3886\(95\)00041-8](https://doi.org/10.1016/0304-3886(95)00041-8).
- [21] Bin Ding and Jianyong Yu. *Electrospun Nanofibers for Energy and Environmental Applications*. Springer, 2014, pp. 497–525. DOI: [10.1007/978-3-642-54160-5_20](https://doi.org/10.1007/978-3-642-54160-5_20).
- [22] Biao Zhang et al. “Recent advances in electrospun carbon nanofibers and their application in electrochemical energy storage”. In: *Progress in Materials Science* 76 (2016), pp. 319–380. DOI: [10.1016/j.pmatsci.2015.08.002](https://doi.org/10.1016/j.pmatsci.2015.08.002).
- [23] J.M Deitzel et al. “The effect of processing variables on the morphology of electrospun nanofibers and textiles”. In: *Polymer* 42.1 (Jan. 2001), pp. 261–272. DOI: [10.1016/S0032-3861\(00\)00250-0](https://doi.org/10.1016/S0032-3861(00)00250-0).
- [24] S. De Vrieze et al. “The effect of temperature and humidity on electrospinning”. In: *Journal of Materials Science* 44.5 (2009), pp. 1357–1362. DOI: [10.1007/s10853-008-3010-6](https://doi.org/10.1007/s10853-008-3010-6).
- [25] Cheryl L. Casper et al. “Controlling surface morphology of electrospun polystyrene fibers: Effect of humidity and molecular weight in the electrospinning process”. In: *Macromolecules* 37.2 (2004), pp. 573–578. DOI: [10.1021/ma0351975](https://doi.org/10.1021/ma0351975).
- [26] W. E. Teo and S. Ramakrishna. “A review on electrospinning design and nanofibre assemblies”. In: *Nanotechnology* 17.14 (2006). DOI: [10.1088/0957-4484/17/14/R01](https://doi.org/10.1088/0957-4484/17/14/R01).
- [27] Zheng Ming Huang et al. “A review on polymer nanofibers by electrospinning and their applications in nanocomposites”. In: *Composites Science and Technology* 63.15 (2003), pp. 2223–2253. DOI: [10.1016/S0266-3538\(03\)00178-7](https://doi.org/10.1016/S0266-3538(03)00178-7).
- [28] Seeram Ramakrishna et al. “Electrospun nanofibers: Solving global issues”. In: *Materials Today* 9.3 (2006), pp. 40–50. DOI: [10.1016/S1369-7021\(06\)71389-X](https://doi.org/10.1016/S1369-7021(06)71389-X).

- [29] Seeram Ramakrishna et al. “Polymer-based composites by electrospinning: Preparation & functionalization with nanocarbons”. In: *Progress in Polymer Science* 86 (2018), pp. 40–84. DOI: [10.1016/j.progpolymsci.2018.07.002](https://doi.org/10.1016/j.progpolymsci.2018.07.002).
- [30] M.S.A. Rahaman, A.F. Ismail, and A. Mustafa. “A review of heat treatment on polyacrylonitrile fiber”. In: *Polymer Degradation and Stability* 92.8 (Aug. 2007), pp. 1421–1432. DOI: [10.1016/j.polymdegradstab.2007.03.023](https://doi.org/10.1016/j.polymdegradstab.2007.03.023).
- [31] Michio Inagaki, Ying Yang, and Feiyu Kang. “Carbon nanofibers prepared via electrospinning”. In: *Advanced Materials* 24.19 (2012), pp. 2547–2566. DOI: [10.1002/adma.201104940](https://doi.org/10.1002/adma.201104940).
- [32] M. M. Coleman and R. J. Petcavich. “Fourier Transform Infrared Studies on the Thermal Degradation of Polyacrylonitrile.” In: *J Polym Sci Polym Phys Ed* 16.5 (1978), pp. 821–832. DOI: [10.1002/pol.1978.180160507](https://doi.org/10.1002/pol.1978.180160507).
- [33] Ko Tse-Hao, Ting Hsing-Yie, and Lin Chung-Hua. “Thermal stabilization of polyacrylonitrile fibres”. In: *Journal of Applied Polymer Science* 35.3 (1988), pp. 631–640. DOI: [10.1016/S0032-3861\(98\)00778-2](https://doi.org/10.1016/S0032-3861(98)00778-2).
- [34] Shahram Arbab et al. “Optimum stabilization processing parameters for polyacrylonitrile-based carbon nanofibers and their difference with carbon (micro) fibers”. In: *Polymer Degradation and Stability* 142 (2017), pp. 198–208. DOI: [10.1016/j.polymdegradstab.2017.06.026](https://doi.org/10.1016/j.polymdegradstab.2017.06.026).
- [35] Meiyu Wu et al. “Optimization of stabilization conditions for electrospun polyacrylonitrile nanofibers”. In: *Polymer Degradation and Stability* 97.8 (2012), pp. 1511–1519. DOI: [10.1016/j.polymdegradstab.2012.05.001](https://doi.org/10.1016/j.polymdegradstab.2012.05.001).
- [36] Yi Peng et al. “Electrospun Li₃V₂(PO₄)₃ nanocubes/carbon nanofibers as free-standing cathodes for high-performance lithium-ion batteries”. In: *Journal of Materials Chemistry A* 7.24 (2019), pp. 14681–14688. DOI: [10.1039/c9ta02740h](https://doi.org/10.1039/c9ta02740h).
- [37] Shicheng Yu et al. “Self-standing NASICON-type electrodes with high mass loading for fast-cycling all-phosphate sodium-ion batteries”. In: *Journal of Materials Chemistry A* 6.37 (2018), pp. 18304–18317. DOI: [10.1039/c8ta07313a](https://doi.org/10.1039/c8ta07313a).
- [38] Ting Jin et al. “Electrospun NaVPO₄F/C Nanofibers as Self-Standing Cathode Material for Ultralong Cycle Life Na-Ion Batteries”. In: *Advanced Energy Materials* 7.15 (2017). DOI: [10.1002/aenm.201700087](https://doi.org/10.1002/aenm.201700087).
- [39] Biao Zhang et al. “Correlation Between Atomic Structure and Electrochemical Performance of Anodes Made from Electrospun Carbon Nanofiber Films”. In: *Advanced Energy Materials* 4.7 (May 2014), p. 1301448. DOI: [10.1002/aenm.201301448](https://doi.org/10.1002/aenm.201301448).
- [40] Yongchang Liu, Fanfan Wang, and Li Zhen Fan. “Self-standing Na-storage anode of Fe₂O₃ nanodots encapsulated in porous N-doped carbon nanofibers with ultra-high cyclic stability”. In: *Nano Research* 11.8 (2018), pp. 4026–4037. DOI: [10.1007/s12274-018-1985-0](https://doi.org/10.1007/s12274-018-1985-0).
- [41] Renzhong Chen et al. “Facile fabrication of foldable electrospun polyacrylonitrile-based carbon nanofibers for flexible lithium-ion batteries”. In: *Journal of Materials Chemistry A* 5.25 (2017), pp. 12914–12921. DOI: [10.1039/c7ta02528a](https://doi.org/10.1039/c7ta02528a).
- [42] Hui Li et al. “Budding willow branches shaped Na₃V₂(PO₄)₃/C nanofibers synthesized via an electrospinning technique and used as cathode material for sodium ion batteries”. In: *Journal of Power Sources* 273 (2015), pp. 784–792. DOI: [10.1016/j.jpowsour.2014.09.153](https://doi.org/10.1016/j.jpowsour.2014.09.153).
- [43] Hua-Kun Liu et al. “Na₃V₂(PO₄)₃ particles partly embedded in carbon nanofibers with superb kinetics for ultra-high power sodium ion batteries”. In: *Journal of Materials Chemistry A* 3.3 (2014), pp. 1005–1009. DOI: [10.1039/c4ta06001f](https://doi.org/10.1039/c4ta06001f).

- [44] Ling Wu et al. “Controllable Synthesis of $\text{Na}_3\text{V}_2(\text{PO}_4)_3/\text{C}$ Nanofibers as Cathode Material for Sodium-Ion Batteries by Electrostatic Spinning”. In: *Frontiers in Chemistry* 6.December (2018), pp. 1–9. DOI: [10.3389/fchem.2018.00617](https://doi.org/10.3389/fchem.2018.00617).
- [45] Jacopo Celè. “Study of the Effect of Carbon Nanofibers Electrodes Morphology on Sodium-ion Cells Electrochemical Performances”. MA thesis. Politecnico di Torino, 2019.

Chapter 2

Materials and Methods

This chapter explains the experimental setups, materials and characterization techniques used in this work. Section 2.1 present the electrospinning setup and the relevant parameters values, stabilization and carbonization procedures and methods used to characterize mat thickness and electrical conductivity. Section 2.2 gives a brief overview of the morphological, structural and compositional characterization techniques employed.

2.1 Electrospinning and Production of CNF

Setup and Spinning Solution

The process flow to fabricate CNF support is shown in Figure 2.1. Fiber mat (white) is spun, then stabilized (brown) and punched with 12 mm hand puncher and eventually carbonized to obtain circular CNF support of ~ 10 mm diameter that can fit in the test cell. P2 indicates the second process flow of NVP loading, described in [1].

A handmade electrospinning setup was used to produce all the fibers used in this work. Setup schematic is shown in Figure(2.2). The high voltage power supply was a Stanford Research System PS300 with maximum output voltage of 20 kV. The needle holder was built using plexiglass hollow pipes. Two holes in the shorter support arm served as needle-holder. The needle was blunt-tipped, 0.80 mm inner diameter, stainless steel. The collectors used were stainless steel plates and aluminum foil. The syringe pump was an Harvard Apparatus PHD Ultra and the syringe was connected to the needle with PTFE connectors and PTFE pipe. A digital camera was used to monitor the spinning process. The setup was placed inside a plexiglass box to control environment parameters. Humidity level was regulated using nitrogen flow inside the box and monitored with a Sensirion humidity sensor. Room temperature was

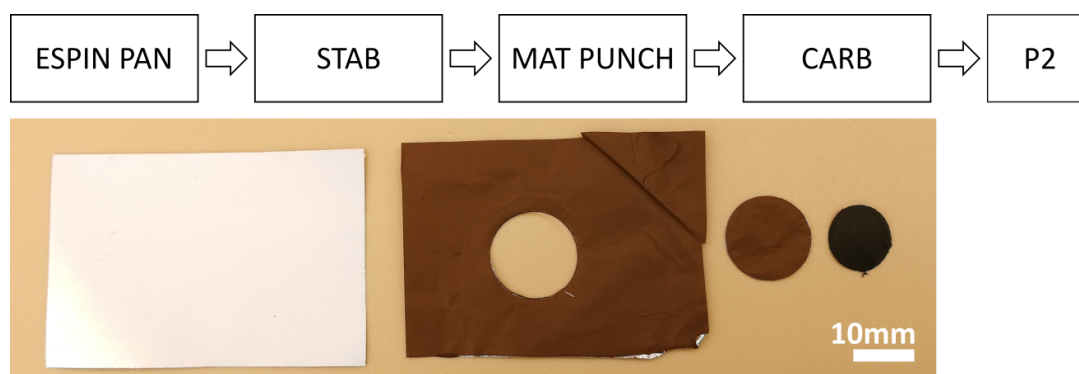


Figure 2.1: Process flow used to produce circular CNF support. The picture represents samples during each phase. P2 is the loading process flow [1].

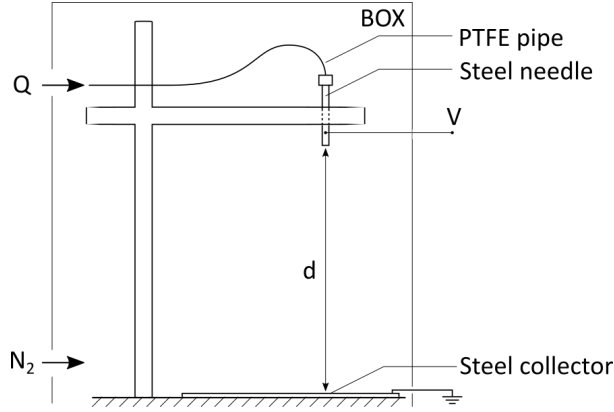


Figure 2.2: Schematics of the electrospinning setup

23 °C for all experiments.

A solution of 8 wt% PAN (Sigma-Aldrich) in DMAc (Sigma-Aldrich) was used to produce all the fibers in this work. PAN was dissolved in DMAc and stirred at 60 °C for 36 h. Solution concentration was taken from [2] and not further optimized.

Electrospinning parameters used for the production of fibers for all the experiments are summarized in Table 2.1.

Parameter	d (cm)	Q (mL h ⁻¹)	V (kV)	RH (%)	T (°C)
Value	15	1.5	14	35	23

Table 2.1: Setup and environment parameters of electrospinning used in this work.

Stabilization and Carbonization Processes

Stabilization temperatures of 200, 230, 260, 280 and 300 °C with dwell time of 1, 1.5 and 2 h were performed to assess optimal temperature and dwell time. Fibers were collected on aluminum foil.

Two stepwise stabilization processes with different temperature ramps and dwell times were also tested in order to assess the effects of slower stabilization on CNF mechanical properties. The maximum plateau temperature was decided after the results of the first stabilization experiment. The two temperature-time profile are reported in Table 2.2. Stabilization processes were all performed in a Thermo Scientific Heraeus oven.

Carbonization was performed in argon atmosphere using a Carbolite tube furnace. Two procedures were used: 900 °C, 2 h, 5 °C min⁻¹ (C1), 800 °C, 8 h, 5 °C min⁻¹ (C2). C1 was used to produce bare CNF after stabilization, as in [2]; C2 was used to anneal NVP particles loaded in CNF prepared with C1. Annealing temperature and time were taken from [3]. Process parameters are summarized in Table 2.3.

Procedure	T_1 (°C)	t_1 (min)	T_2 (°C)	t_2 (min)	T_3 (°C)	t_3 (min)
S1	100	30	200	30	260	120
S2	100	60	-	-	260	120

Table 2.2: Stepwise stabilization procedures with different temperature and dwell times used to assess the effect of a slow treatment on the mechanical properties of CNF.

Procedure	T ($^{\circ}\text{C}$)	t (h)	Rate ($^{\circ}\text{C min}^{-1}$)	Ref.
C1	900	2	5	[2]
C2	800	8	5	[3]

Table 2.3: Carbonization temperatures and dwell times. C1 was used to prepare bare CNF. C2 was used to anneal NVP after CNF loading.

Dependence of Mat Thickness on Spun Solution Volume

Solution volumes of 50, 100, 200, 500, 1000, 2000 μL were spun on steel collector. The central part of the mat was cut and two samples were kept as a reference, one treated with S1, one treated S1-C1. Cross sections were prepared after the thermal treatments by razor blade cut. Sections of S1 and S1-C1 samples were measured with SEM. As spun mats were not measured as they were too soft to be cut with razor blade without causing compressive stress.

Conductivity Measurement

The conductivity of CNF (S1-C1) through and along the mat plane (σ_t, σ_l , transversal and longitudinal, respectively) was evaluated. Two probes measurement was used to measure transversal and longitudinal resistance (R_t, R_l). A schematic of the two setups used and relevant quantities are shown in Figure 2.3. Mat thickness (t) was measured from SEM image and was 70 μm . CNF were punched in 10 mm disks. Contacts to the CNF were made with copper tape (resistance $< 0.01 \Omega$) mounted on glass slide. A second glass slide was used to apply uniform pressure on top of the CNF.

Current was swept from -1 mA to 1 mA with a step of 0.10 mA (Keithley 2400 SourceMeter; Keithley 2000 Multimeter for voltage measurement). Data were acquired with a LabView software already available in the laboratory.

Transversal and longitudinal resistance were extracted from the linear fit of V versus I and σ_t, σ_l computed as:

$$\sigma_t = \frac{t}{R_t h_t l_t} \quad \sigma_l = \frac{l_l}{R_l h_l t} \quad (2.1)$$

Mean value and standard deviation were evaluated over five samples (MATLAB).

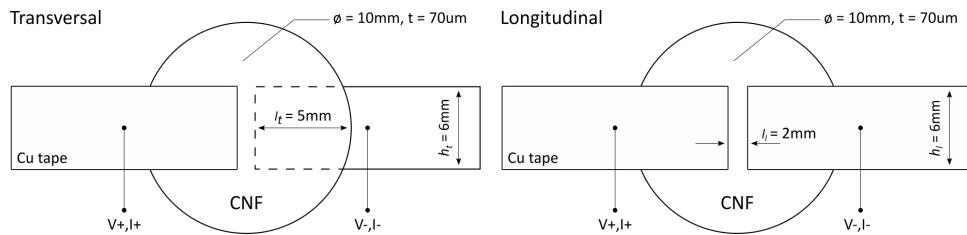


Figure 2.3: Setup for the measurement of transversal and longitudinal resistance of CNF samples. Quantities reported were used to evaluate σ_t, σ_l

2.2 Characterization Techniques

SEM, TEM and EDX

Scanning Electron Microscopy (SEM) is a technique to study the surface and near surface structure of bulk samples. Contrarily to optical microscopes, which exploits photons in the visible range to image an object, the imaging probe in SEM is a beam of electrons (*primary*

beam) with energy (E) comprised between 1 and 30 kV. The De Broglie's relation allows to derive the wavelength (λ) of such electrons:

$$\lambda = \frac{h}{\sqrt{2m_e E}} \quad (2.2)$$

which for the energy range of SEM is of the order of few nanometers (h is the Plank's constant and m_e the electron mass).

Such small wavelength allows to overcome the resolution limit for visible light in optical microscopes imposed by the Rayleigh criteria:

$$\delta = \frac{0.6\lambda}{NA} \quad (2.3)$$

being δ the smallest distance that can be resolved and NA the numerical aperture of the objective lens. SEM can thus image the surface of an object with a resolution as low as 10 nm.

Furthermore, when primary beam electrons (PE) hit the sample, a wide range of secondary electrons are generated (Figure 2.4) [4, 5]. These are collected by SEM detectors and the signal is converted into an image by digital processing. Secondary electrons (SE) are the most used to create SEM images and they provide information about surface morphology. Backscattered electrons (BSE) are generated by PE elastically scattered by heavy elements and can thus provide a qualitative compositional analysis by image contrast. If the energy of PE is sufficiently high, inner shell electrons of the sample atoms can be ejected. The formed hole is filled by an electron of higher energy shells and a characteristic X-Ray photon is emitted. The analysis of such X-Rays is performed by Energy Dispersive X-ray Spectroscopy (EDX) through which chemical characterization of the sample is possible. SEM samples do not require any particular preparation but, in case on non conductive materials, a thin conductive coating is necessary to prevent accumulation of charges on the sample surface and shielding of the PE beam.

Transmission Electron Microscopy (TEM) is conceptually similar to SEM but the PE used are highly energetic, up to 200 kV and the information is generated by the collection of electrons transmitted (TE) through the sample, either elastically or inelastically (ESE,ISE), resulting in a 2D image. A wavelength of few picometers endows TEM with resolution power of less than 10 nm and, being λ comparable with inter atomic spacing, allows TEM electrons to produce diffraction patterns when crystalline or polycrystalline samples are observed, This features is fundamental to assess material phase and the presence of defects. TEM samples require special preparation as they need to be thinned down to few tens of nanometers.

Zeiss Gemini 300 SEM was used for SEM imaging and EDX. Samples were coated with 5 nm thick sputtered carbon. FEI Talos TEM was used for TEM imaging and EDX on CNF/NVP powder sample. Powder was disperse in ethanol an dropped on copper support grid. Information about SEM and TEM parameters are reported in the images presented in (ch results)

XRD

X-Ray Diffraction (XRD) is an analytical technique to determine the structure of crystalline materials [6]. X-Ray photons with energies of about 10 kV have wavelengths of the order the inter atomic spacing ($\sim 1 \text{ \AA}$) and therefore characteristic diffraction patterns arise when an X-Ray beam impinges on a crystalline sample. XRD can be explained using Bragg's model, were the incident beam is scattered by lattice ions arranged in families of parallel planes, identified by the Miller's indexes h, k, l , spaced by a distance d_{hkl} (Figure 3.10a). If θ is the incidence angle, a distinctive intensity peak of the reflected beam will be observable only for those planes that generate constructive interference. There is thus a relation between the probe characteristics (λ, θ) and the crystal structure (d_{hkl}), formally given by the Bragg's law:

$$n\lambda = 2d_{hkl}\sin\theta \quad (2.4)$$

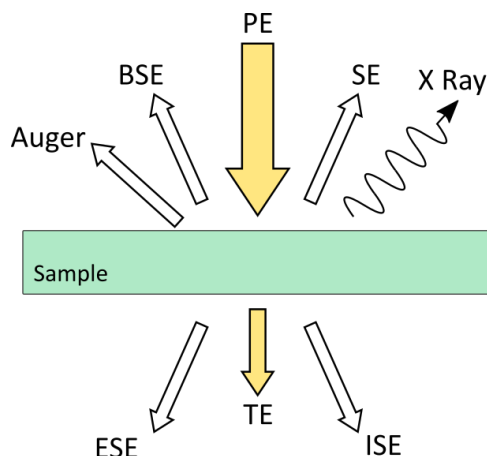


Figure 2.4: Electrons generated upon incidence of primary electrons beam (PE) in SEM and TEM. SEM: secondary electrons (SE), backscattered electrons (BSE), characteristic X-Ray and Auger electrons. TEM: transmitted electrons (TE), elastically and inelastically scattered electrons (ESE,ISE).

n is the diffraction order namely the position of intensity maxima of scattered beams with respect to the non scattered beam (zeroth order), which is transmitted through the sample. One can thus recover information about the sample crystal structure by varying λ and θ and detecting the diffracted peak position and intensity.

If the phase of a sample is not known, XRD on pulverized sample is used to assess whether crystalline, polycrystalline or amorphous phases are present. For powder samples, a random distribution of all the possible crystal orientation (if any) is assumed. In such a way all the different families of planes can be looked for by changing θ . The common set up is called Bragg-Brentano (Figure 3.10b) and consists of an X-Ray source which can rotate of an angle θ , a sample holder and a detector which is scan simultaneously with the beam source in order to keep always the same angle θ from the holder plane.

Powder XRD spectrum gives thus information about the presence of crystalline phases, their relative amount and the (hkl) plane that generated a certain peak. Powder XRD was conducted

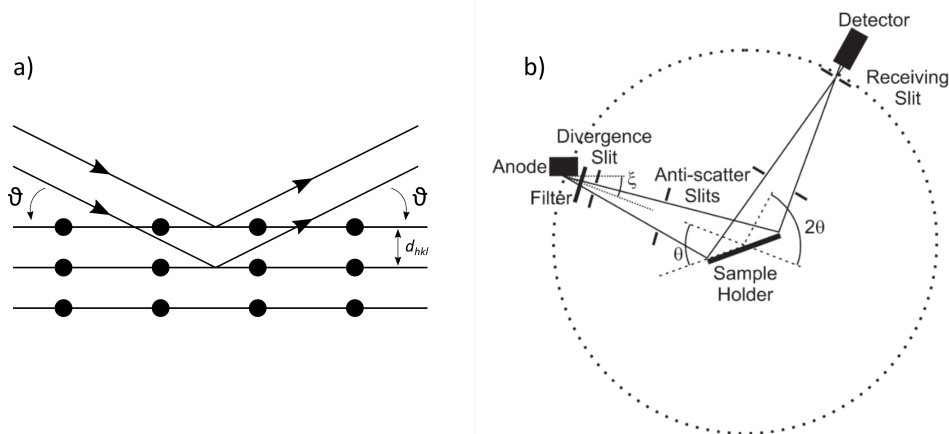


Figure 2.5: a) Bragg's model to explain diffraction from crystal planes. b) Typical Bragg-Brentano setup for powder XRD (taken from [6]).

with a PANalytical Empyrean scanning from 10° to 90° .

FTIR

Fourier Transform Infrared Spectroscopy (FTIR) is an analytical technique to characterize the molecular structure of a sample through its infrared (IR) absorbance spectrum [7]. IR radiation

has wavelength (λ_{IR}) ranging from 750 nm to 1 mm and the corresponding energy is suitable to excite the quantized vibrational states of a molecule. It is common use in FTIR to express λ_{IR} in terms of wavenumber $k = 2\pi/\lambda_{IR}$. Generally, the IR beam impinges on the sample and its wavelength is swept in the mid-infrared range ($400 - 4000 \text{ cm}^{-1}$), where most of the vibrational modes lie. The intensity of the transmitted beam is recorded and peaks in the transmission-wavelength spectrum appears in correspondence of characteristic wavelengths which can then be associated to particular chemical bonds and functional groups.

In FTIR the incident beam is polychromatic and is passed through a Michelson interferometer before hitting the sample. The interferometer allows to rapidly scan through all the λ composing the spectrum, resulting in a faster and better resolved measurement compared to simple transmission IR spectroscopy.

When only thin or irregular samples are available, possibly resulting in too low absorption, Attenuated Total Reflectance (ATR) FTIR is exploited to obtain fast measurements with little sample preparation. ATR exploits total internal reflection of the IR beam caused by the interface between an *internal reflection element* (IRE, usually Ge or ZnSe prisms) of high refractive index and the sample. The evanescent wave excites the vibrational modes and the output beam is collected and used to generate the absorbance-wavelength spectrum (Figure 2.6a).

The FTIR used was a Nicolet 6700 in ATR mode. Scans were acquired from 600 to 4000 cm^{-1} . Baseline removal and peaks match were performed with Nicolet software. Spectra used for comparison among different stabilization temperatures were scaled by a common factor for better highlighting relevant peaks.

Raman Spectroscopy

Similarly to FTIR, Raman spectroscopy probes the vibrational states of organic and inorganic compounds by exploiting an incident light beam in the visible range. Information about the sample chemical composition, as well as details about phononic bands for crystalline and polycrystalline materials and vibrational modes for molecular compounds are obtained by detecting inelastically scattered light. As a consequence of light-matter interaction, impinging photons can lose or gain energy by interacting with vibrational states. This interaction is particularly strong for carbon based materials, thus Raman spectroscopy is widely exploited to gain information about hybridization states of carbon, crystallite size, presence of defects and graphitization level [8]. Figure 2.6b shows examples of Raman spectra for different carbon structures, highlighting how crystalline order and defects affect the spectra in a distinctive way, thus providing a unique fingerprint. Two remarkable features are the bands at 1580 cm^{-1} and 1350 cm^{-1} . These are respectively called G and D band. The G band is characteristic of sp^2 carbon in graphite (G for graphite) and it has high intensity in highly ordered pyrolytic graphite (HOPG) or in other structure having a certain degree of graphitization, for examples CNF. The D band arises in samples with defects and disordered structures (D for defects). The ratio between D and G band intensities (I_D/I_G) is used to quantify the quality of a carbon structure. A low ratio implies a higher graphitization level and thus a more ordered structure.

References

- [1] Jacopo Celè. “Study of the Effect of Carbon Nanofibers Electrodes Morphology on Sodium-ion Cells Electrochemical Performances”. MA thesis. Politecnico di Torino, 2019.
- [2] Qiongjuan Duan et al. “Fabrication of a carbon nanofiber sheet as a micro-porous layer for proton exchange membrane fuel cells”. In: *Journal of Power Sources* 195.24 (2010), pp. 8189–8193. DOI: [10.1016/j.jpowsour.2010.07.032](https://doi.org/10.1016/j.jpowsour.2010.07.032).

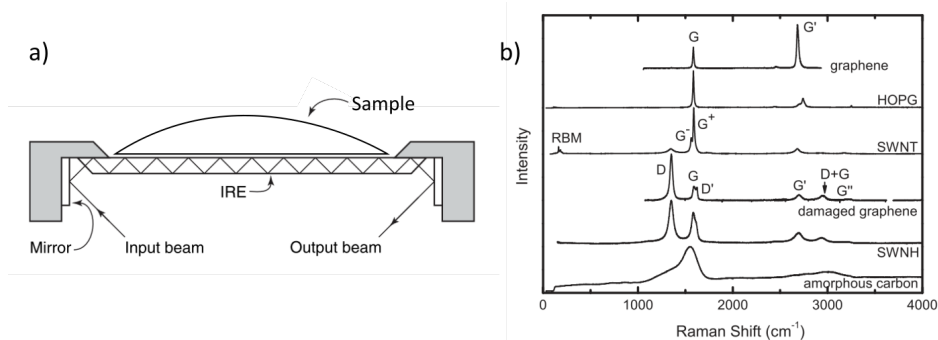


Figure 2.6: a) Schematics of FTIR in ATR mode. Adapted from [7]. b) Examples of typical Raman spectra of different carbon structures. Taken from [8].

- [3] Shicheng Yu et al. “Self-standing NASICON-type electrodes with high mass loading for fast-cycling all-phosphate sodium-ion batteries”. In: *Journal of Materials Chemistry A* 6.37 (2018), pp. 18304–18317. DOI: [10.1039/c8ta07313a](https://doi.org/10.1039/c8ta07313a).
- [4] David B. Williams and C. Barry Carter. *Transmission Electron Microscopy: a Textbook for Materials Science*. Second. September. Springer, 2009, p. 9.
- [5] Peter J. Goodhew, J. Humphreys, and Richard Beanland. *Electron Microscopy and Analysis*. Third. London: Taylor & Francis, 2001.
- [6] S J L Billinge and R E Dinnebier. *Powder Diffraction: Theory and Practice*. RSC Publishing, 2008, p. 302.
- [7] Peter R. Griffiths and J. A de Haseth. *Fourier Transform Infrared Spectrometry*. Second. Wiley, 2007. DOI: [10.1007/978-3-642-11274-4_3256](https://doi.org/10.1007/978-3-642-11274-4_3256).
- [8] Ado Jorio et al. *Raman Spectroscopy in Graphene Related Systems*. Wiley-VCH, 2011. DOI: [10.1002/9783527632695.ch14](https://doi.org/10.1002/9783527632695.ch14).

Chapter 3

Results and Discussion

The main results concerning the production of spun PAN mats and successive treatments to obtain CNF are reported in this chapter. Section 3.1 present the morphology of mats, fibers diameter and the SEM analysis of mat cross section. Section 3.2 summarize the results of experiments performed to evaluate mat thickness as a function of the solution rate. Section 3.3 is concerned with the assessment via FTIR of the stabilization procedure and its role in yielding final CNF with good morphology. Section 3.4 shows the outcome of the carbonization step, the structural composition of CNF evaluated by XRD, TEM and Raman spectroscopy and the result of conductivity measurements.

3.1 Fibers and Mats: Morphology after Spinning, Stabilization and Carbonization

The electrospun PAN mat covered a circular area of about 10 cm on the steel collector during the spinning process. After being peeled off, the mat was soft, bendable and easy to cut (Figure 3.1a,b). SEM imaging of the mat surface showed PAN fibers with circular cross section, distributed randomly and forming a non-woven texture with pores in the micron range determined by inter-fibers spacing and superposition (Figure 3.1c). Average diameter was 318(83) nm, compatible with the value obtained for the same PAN/DMAc solution and similar setup by [1].

Morphology of the fiber was not affected after stabilization (S1) and diameter was not altered, with an average value of 341(47) nm.

Average diameter reduced to 173(14) nm after carbonization (C1), 45% of the pre carbonization value. Weight loss of about 50% was also observed after carbonization. Both results were attributed to nitrogen and hydrogen loss during high temperature treatment (see Section 1.3)

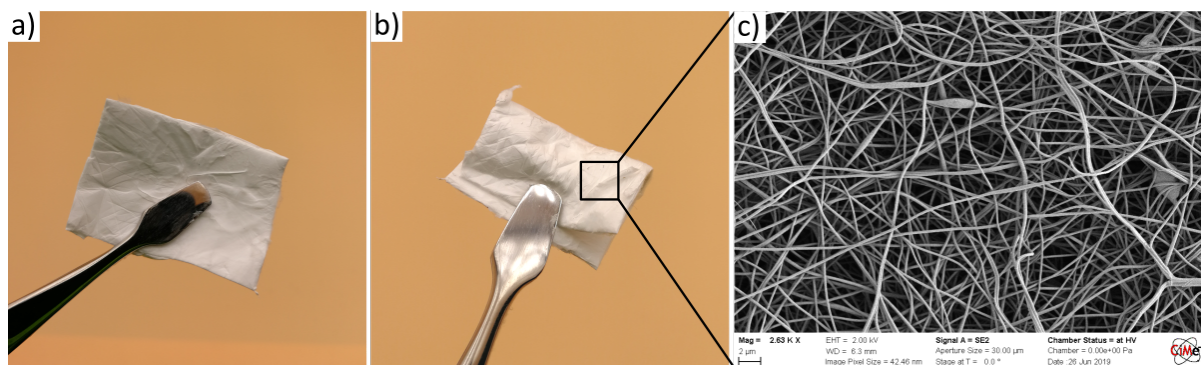


Figure 3.1: a) PAN mat produced by electrospinning and the cut. b) Bended PAN mat showing high flexibility. c) SEM image of mat surface, showing PAN fibers randomly oriented, arranged in a non woven structure.

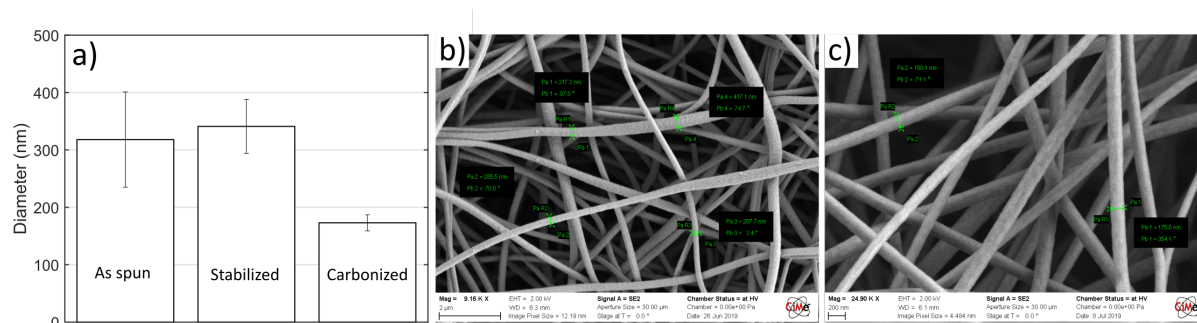


Figure 3.2: a) Average diameter variation for as spun, stabilized and carbonized fibers. b) Example of SEM image of as spun fibers used for diameter measurement c) Example of SEM image of carbonized fibers used for diameter measurement.

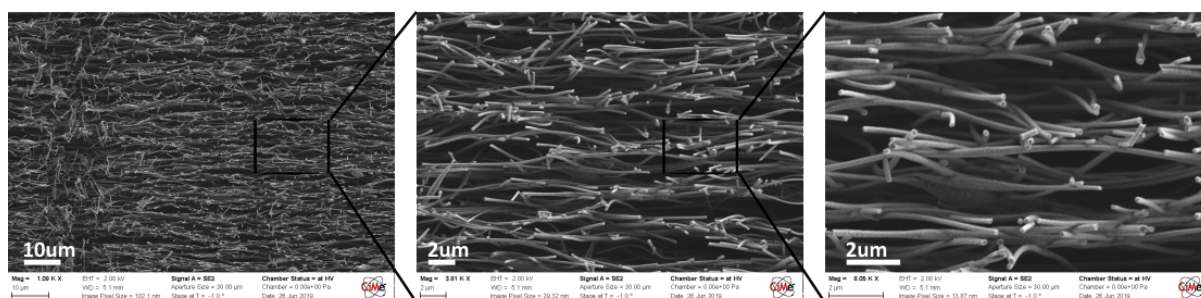


Figure 3.3: SEM image of a CNF cross section. Porosity and fiber sheets are visible along the whole thickness.

[2]. Variation of average diameter during process steps is sum up in Figure 3.2a. Close up on as spun and carbonized fibers are reported in Figure 3.2b,c.

Mat cross section revealed a structure formed by the stacking of several sheets composed of randomly oriented fibers. Cavities were formed where fiber sheets had no contact between each other, resulting in a series of interconnected pores homogeneously distributed along the section (Figure 3.3). No significative difference between cross sections morphologies of stabilized and carbonized mats was observed, both for thin (50 μm) and thick (1 mm) mats (Figure 3.4). This sponge-like morphology is ideal to enable optimal percolation paths for the electrolyte inside mats, regardless of their thicknesses.

EDX analysis conducted on a sample loaded with NVP (see J.Celè [3]) confirmed the chemical composition of the fibers, carbon being uniformly distributed along the section (Figure 3.5). Oxygen and sodium were present due to the loading of active material. Only traces of vanadium and phosphorous were revealed, probably due to non homogeneity in the loading or in the precursor solution concentration. Traces of Ca and Si were imputed to contaminations. Further SEM of mat and fiber morphology is reported in the Appendix 5.

3.2 Dependence of Mat Thickness on Volume of Spun Solution

Mat thickness is a crucial parameter for an electrode support. A thick mat can host a higher amount of active material therefore increasing the cell energy, provided that electrolyte diffusion is optimal throughout the entire thickness. In that case, every particle of active material can be reached by the electrolyte and less underutilization is expected if compared to slurry-based electrodes (Section 1.2).

The dependence of mat thickness on the volume of spun solution was studied in order to better characterize the spinning apparatus. Figure 3.6 shows the results for mats before and after carbonization. Thickness grew rapidly up to 500 μL of spun solution, then linearly up to 1 mL

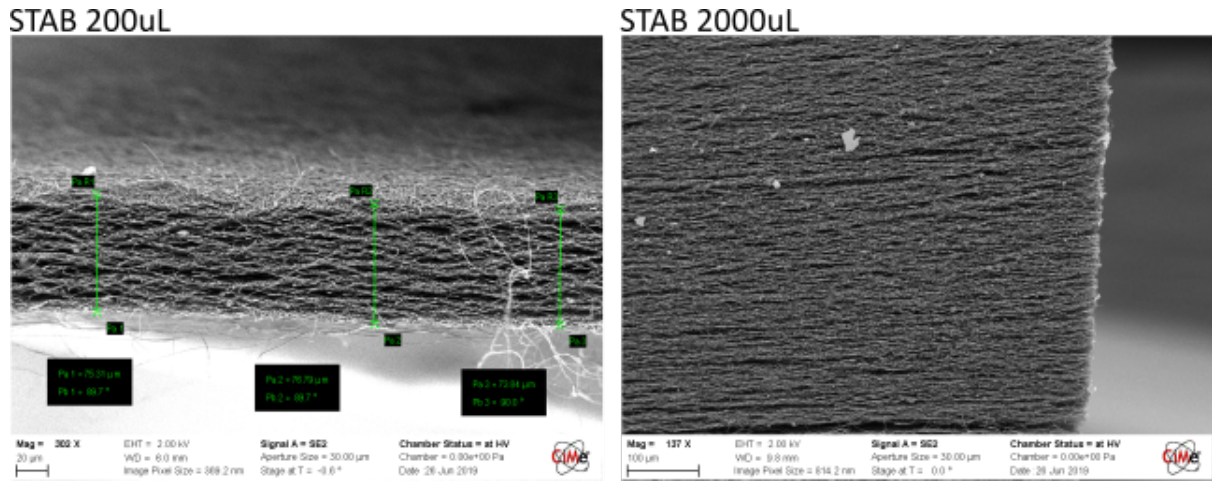


Figure 3.4: SEM cross sections of stabilized mat spun with 200 and 2000 μL . No major morphological differences are visible along the mat section.

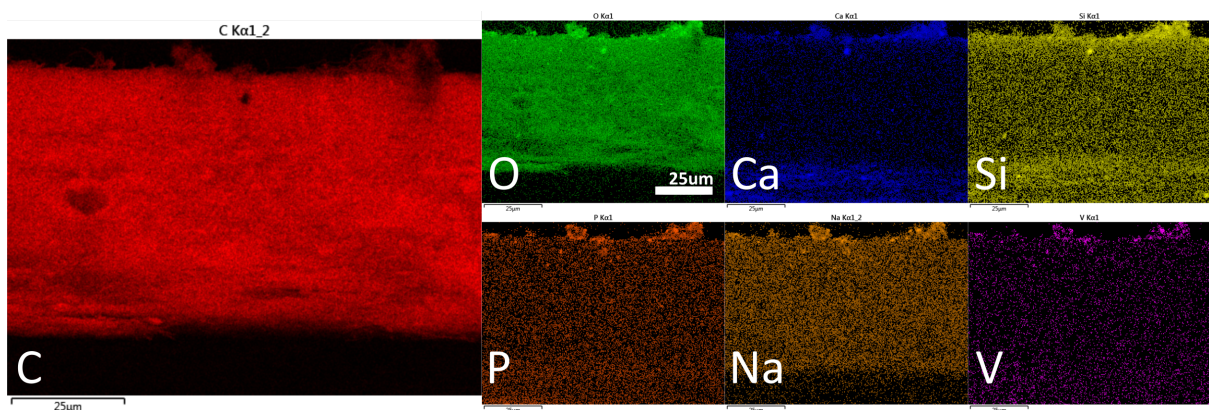


Figure 3.5: Cross section EDX analysis of a CNF loaded with NVP. Carbon was present uniformly along the mat section. O, Na,P and V are due to NVP loading. Traces of contaminating Ca and Si are revealed.

and eventually slowed down for further volume increase. During the initial phase of the spinning process, a high number of fibers are deposited close to the central area of the collector. As spinning continues, the central area grows thicker than the peripheral region [4]. Yet, after a certain thickness, electrostatic repulsion exerted by the already deposited mat on the new fibers may cause deposition to progress more on the peripheral region than on the central part. A thick mat could prevent surface fibers to fully discharge, thus enough electrostatic charges could still be present of the surface layers. This could explain the slower growth of the mat after a certain solution volume.

As future perspective, statistical analysis should be carried out on pre and post carbonization samples in order to develop supports with controllable and reproducible thicknesses. So far, few studies have been conducted on mat thickness growth [4] and the most recent works report CNF electrode support with thickness ranging only from 40 to 150 μm [5, 6], without any reference to the effect on cell performances.

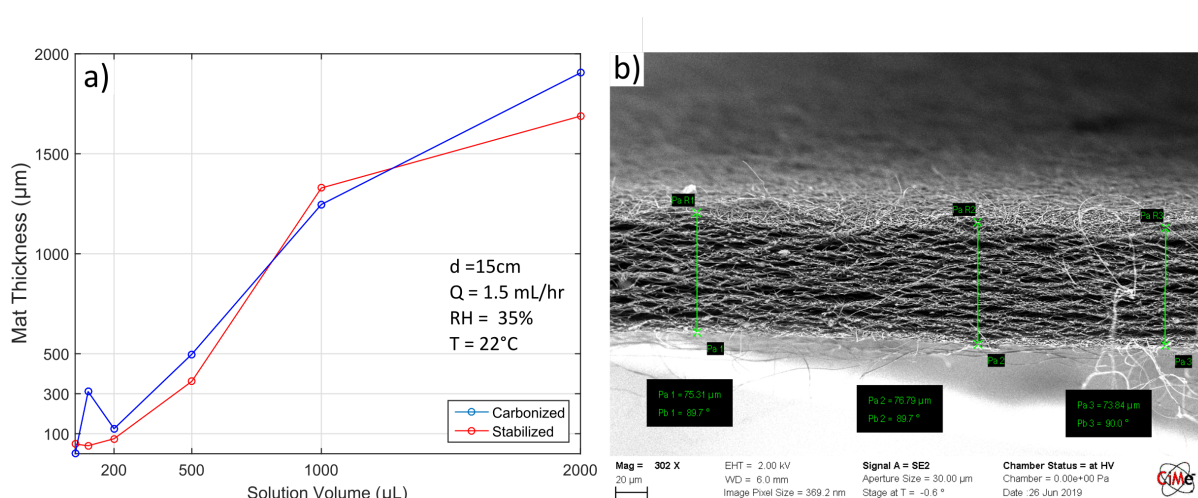


Figure 3.6: a) Dependence of mat thickness on volume of spun solution for stabilized and carbonized fibers b) Example of SEM image used to measure the thickness of a stabilized sample.

3.3 Assessment of Stabilization via FTIR

The stabilization process was analyzed with FTIR to assess optimal temperature and time. Figure 3.7a shows the evolution of absorbance spectrum for fibers stabilized at 260 $^\circ\text{C}$ for different times. The main molecular groups useful to determine the stabilization chemistry state are highlighted.

The spectrum of fibers before stabilization (lower curve) was the one of pure PAN and it was characterized by peaks at 2937 cm^{-1} , 2242 cm^{-1} and 1452 cm^{-1} , assigned to C-H, C \equiv N and CH₂, respectively [7, 8, 9]. The strong peak at 1629 cm^{-1} , detectable only in the mat before stabilization, was assigned to the C=O of DMAc, meaning that part of the solvent was still present in the mat and fully removed only upon stabilization¹.

The transformation of PAN molecule developed as described in Section 1.3 and was confirmed by the reduction of C-H, C \equiv N and CH₂ peaks and the arising of strong peaks at 1581 cm^{-1} (C=C and C=N) and 1363 cm^{-1} (C=N) [7, 8, 9]. Sample colour turned from light to dark brown as stabilization temperature increased (Figure 3.7b, sideways.), transformation due to the formation of ring structures in PAN molecule [10, 9]. The spectra of samples stabilized at different temperatures for 2 h are compared in Figure 3.7b. All major peaks disappeared at 260 $^\circ\text{C}$, 280 $^\circ\text{C}$ and 3000 $^\circ\text{C}$ but elimination of C \equiv N was more complete at 280 $^\circ\text{C}$ and 3000 $^\circ\text{C}$. Yet, since

¹As DMAc is reported to be highly toxic and part of it is still present in the mat after spinning. It is thus necessary to let it evaporate under the fume hood before handling the mat any further.

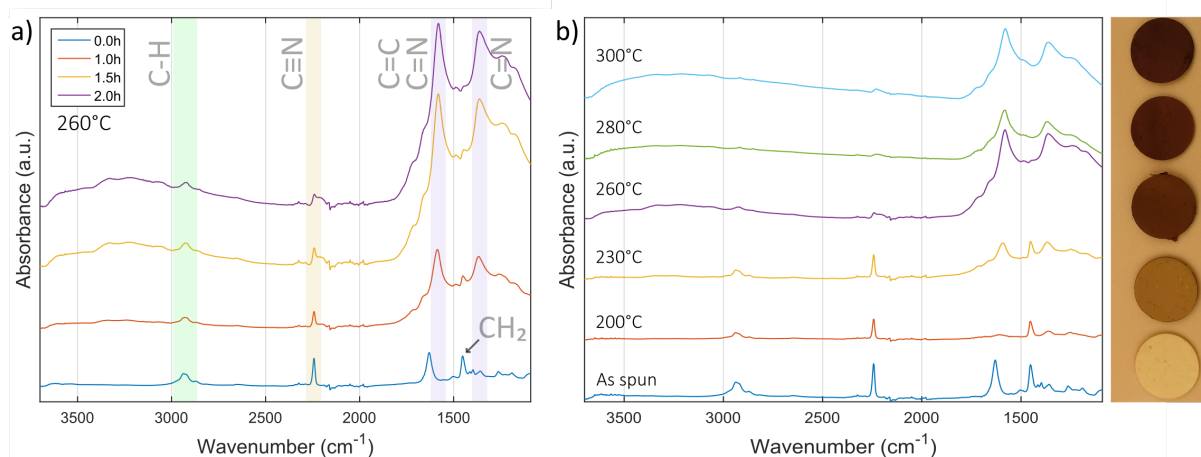


Figure 3.7: a) FTIR spectra of fibers stabilized at 260 °C for 1, 1.5 and 2 h. Spectrum of as spun fibers reported as 0.00 h. Relevant peaks for PAN and PAN stabilization are highlighted. b) FTIR spectra of fibers stabilized for 2 h at 200, 230, 260, 280 and 300 °C. On the side, colour variation of samples stabilized at 200, 230, 260, 280 and 300 °C (bottom to top).

no remarkable differences were observed among the three spectra, a maximum stabilization temperature of 260 °C was used for the production of all the CNF in this work in order to reduce the overall stabilization time. For comparison purpose, a sample of fiber stabilized at 200 °C for 2 h was carbonized (C1) in order to analyze the effects of a poor stabilization on the final CNF morphology. Even if some superficial fibers still retained their morphology, a continuous and homogeneous background of melted PAN was visible (Figure 3.8, green insets and Figure 3.8) confirming the destructive effects of incomplete stabilization on fibers morphology and mat porosity [2, 11]. Further FTIR spectra are reported in the Appendix 5.

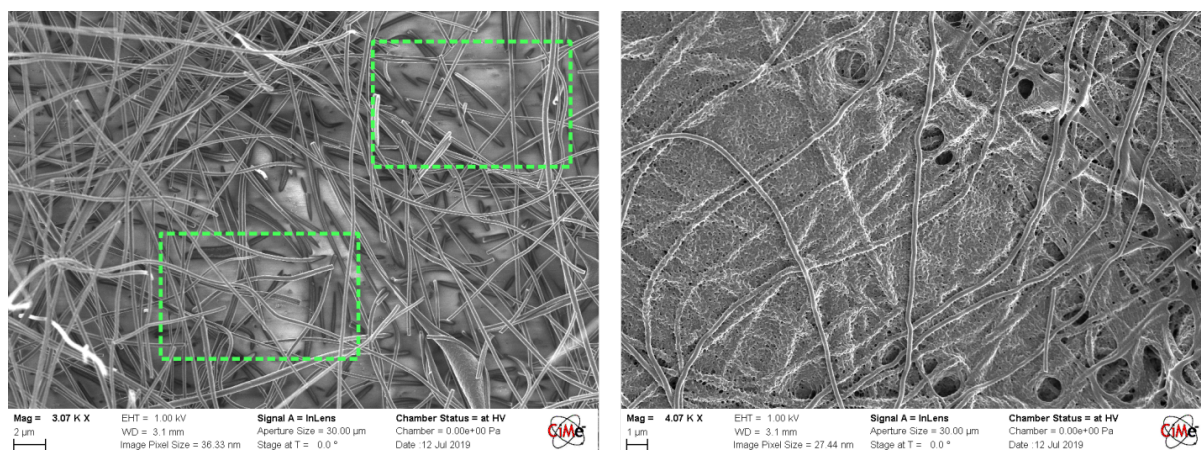


Figure 3.8: Effect of incomplete stabilization of CNF morphology. Green insets highlight melted PAN background.

3.4 Carbonization and its Effects on CNF Structure and Conductivity

CNF prepared with process S1-C1 showed good mechanical stability and could be handled without cracking. Stabilized mats were punched with a 12 mm hand puncher, yielding circular CNF with a reduced diameter of ~ 10 mm. A typical circular CNF sample is presented in Figure 3.9 together with cross section SEM image. The XRD conducted on CNF/NVP powder sample revealed carbon peaks around $27^\circ(2\theta)$ and $45^\circ(2\theta)$, associated with diffraction from the (002)

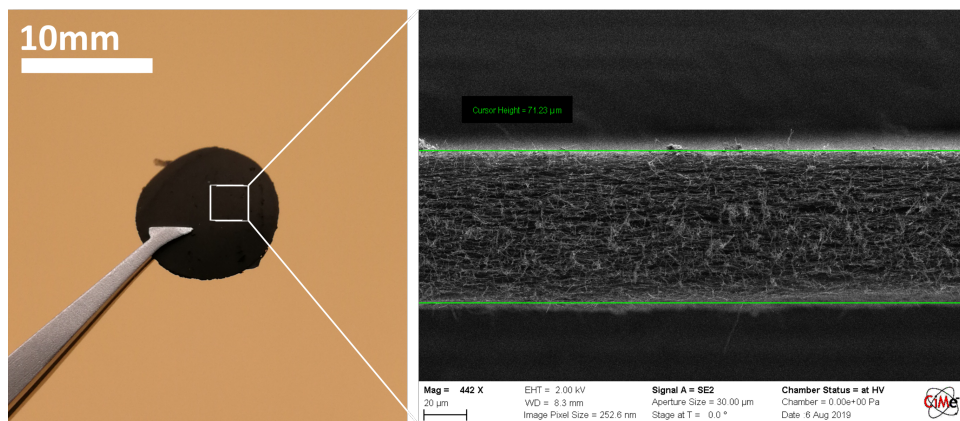


Figure 3.9: Circular CNF and its cross section SEM image

and (100) planes, respectively (Figure 3.10). [1, 12, 13, 14]. The presence of diffraction peaks indicated that CNF treated with procedure C1 underwent partial crystalline reordering, further confirmed by TEM analysis.

Fiber was almost entirely amorphous (Figure 3.12a,b) yet the presence of graphite layers arranged in domains of few tens of nanometers were visible close to the surface (Figure 3.12c), indicating the coexistence of an amorphous and polycrystalline phase in the CNF. The interlayer spacing was about 0.322(58) nm, compatible with the value of (0.33 nm), calculated for the 27° (2θ) peak with Bragg's law. All the other peaks were successfully associated with the rhombohedral lattice of NVP and are reported in the Appendix 5 and detailed in [3].

EDX analysis on the CNF/NVP powder sample revealed expected carbon composition of the single CNF and of the NVP nanoparticle (Figure 3.13). Raman spectroscopy provided further

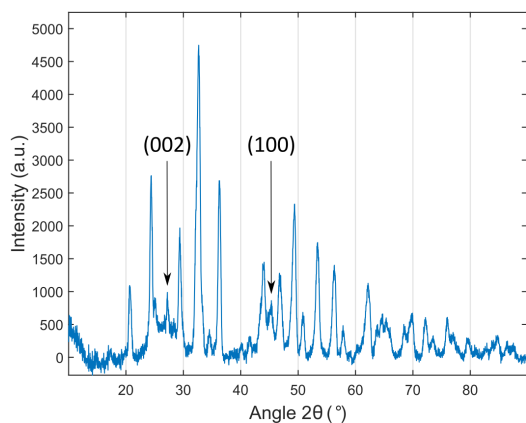
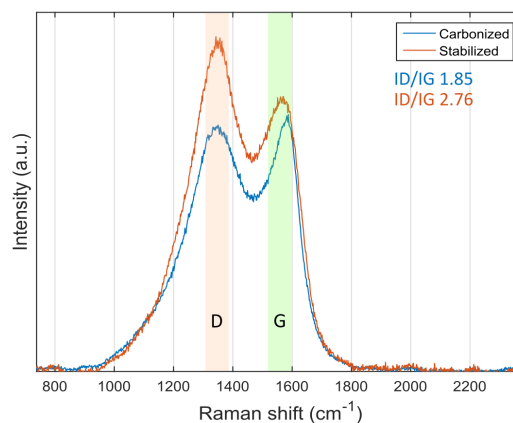


Figure 3.10: XRD spectrum of CNF/NVP powder. Marked peaks were assigned to (002) and (001) carbon planes.

Figure 3.11: Raman spectra of stabilized and carbonized fibers. Reduction I_D/I_G of ratio after carbonization indicated reduction of defect sites.

information about the transformation of fiber structure upon carbonization. Figure 3.11 reports the Raman spectra of stabilized (S1) and carbonized (C1) fibers. Peaks at 1342 cm^{-1} and 1579 cm^{-1} for the CNF were identified as D and G bands of carbon [13, 12, 15]. Both bands were also well visible in the spectra of stabilized (S1) samples (1346 cm^{-1} and 1569 cm^{-1}). The presence of an intense D band was expected due to the entirely amorphous phase of PAN in spun fibers whereas the existence of a G band was explained by the arising of a graphite-like structure in PAN molecule during stabilization (1.3) [16, 15]. The D band is characteristic of carbonaceous structures having defects or a highly disordered state, either determined by the amorphous phase or by the presence of many small crystalline domains and the related high number of domain

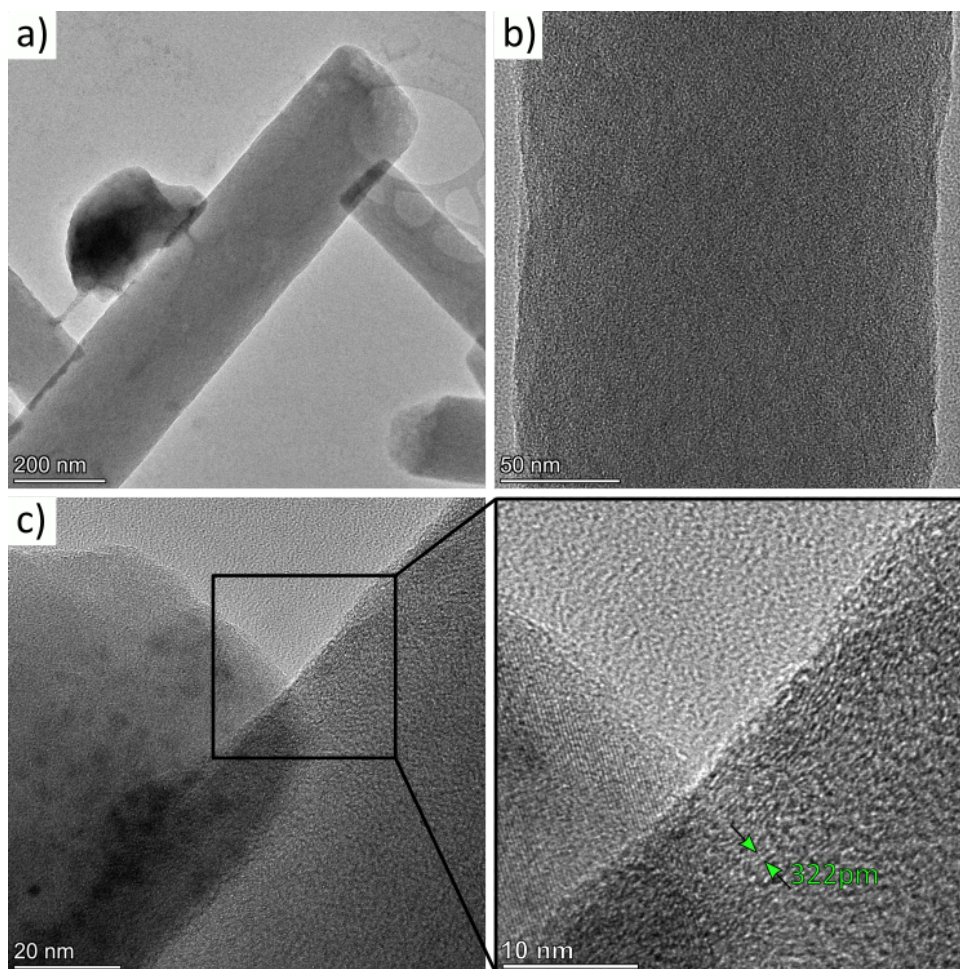


Figure 3.12: TEM images of CNF: a) CNF with NVP particle on the surface. b) CNF core showing the amorphous phase. c) Close up on CNF surface, showing polycrystalline order due to existence of small graphite domains. Measured interlayer spacing of 322 pm shown on the image.

boundaries in the case of polycrystalline samples. G band is instead distinctive of materials with a certain extent of graphitic structure.

Reduction of I_D/I_G ratio from 2.76 to 1.85 after carbonization suggested that carbon underwent a slight phase transition during which amorphous phase recovered a polycrystalline order in the form of graphitic domains, as supported by TEM analysis (Figure 3.12c). Fibers with partial graphitic structure, as the one produced in this work, have higher electrical conductivity than amorphous ones and can thus better collect and provide electrons from and to the active material as redox reaction progresses. The measured transversal and longitudinal conductivity (σ_t , σ_l) of CNF (S1-C1) were $13(2) \text{ mS cm}^{-1}$ and $423(4) \text{ mS cm}^{-1}$, respectively. The tenfold lower value of σ_t compared to σ_l was probably caused by the reduced contact among fiber sheets along the transversal cross section of the mat, resulting in a higher impedance path. Longitudinal conductivity could instead be favoured by the high interconnection of fibers along the stacked planes.

Longitudinal conductivity value was 100 times lower than the one reported in [1] for process similar to C1 and comparable to values obtained for lower carbonization temperature ($\sim 860 \text{ mS cm}^{-1}$ [17, 12]. The mat was probably damaged during handling due to the reduced thickness. Comparative values of transversal conductivity were not available in literature [17, 12, 1, 9, 18, 19] and the measurement setup is not always reported. It can be reasonably assumed that reported conductivities were measured longitudinally, on the mat plane with conventional four probe stations.

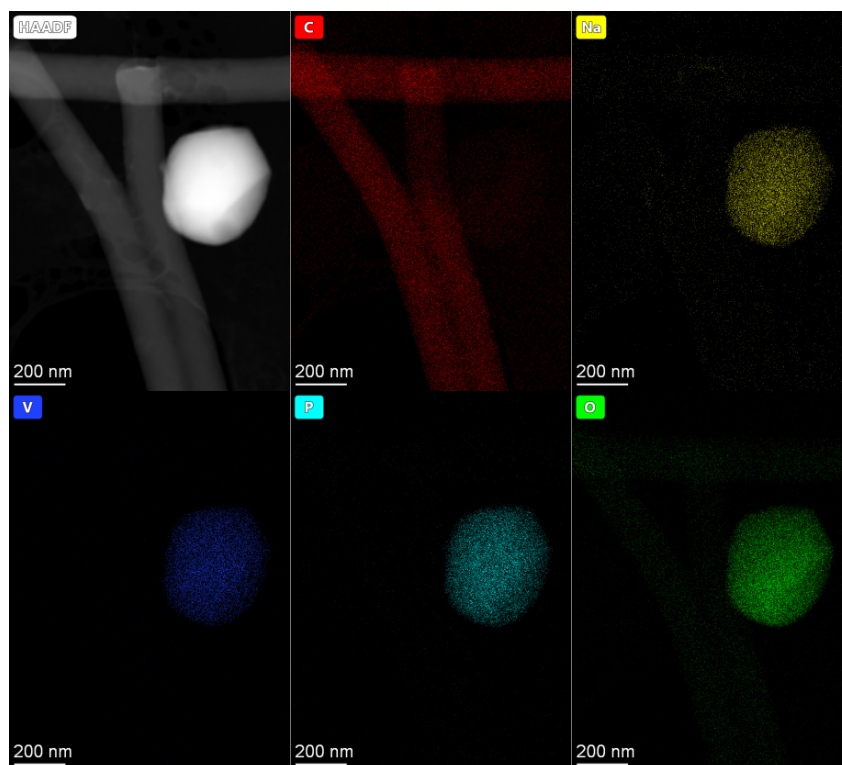


Figure 3.13: EDX analysis on CNF/NVP observed at TEM. Expected composition of CNF and NVP particle was observed.

Conductivity of stabilized fiber (S1) could not be measured as its value exceeded the measurement range. Since the stabilized fiber is still polymeric, its resistivity is expected to be in the order of $1 \text{ M}\Omega\text{cm}$ as reported by [18] for similar samples.

Example of linear fit obtained for transversal and longitudinal measurements are reported in the Appendix 5.

References

- [1] Qiongjuan Duan et al. “Fabrication of a carbon nanofiber sheet as a micro-porous layer for proton exchange membrane fuel cells”. In: *Journal of Power Sources* 195.24 (2010), pp. 8189–8193. DOI: [10.1016/j.jpowsour.2010.07.032](https://doi.org/10.1016/j.jpowsour.2010.07.032).
- [2] Michio Inagaki, Ying Yang, and Feiyu Kang. “Carbon nanofibers prepared via electrospinning”. In: *Advanced Materials* 24.19 (2012), pp. 2547–2566. DOI: [10.1002/adma.201104940](https://doi.org/10.1002/adma.201104940).
- [3] Jacopo Celè. “Study of the Effect of Carbon Nanofibers Electrodes Morphology on Sodium-ion Cells Electrochemical Performances”. MA thesis. Politecnico di Torino, 2019.
- [4] Jongwan Lee, Young Hun Jeong, and Dong Woo Cho. “Fabrication of nanofibrous mats with uniform thickness and fiber density”. In: *Macromolecular Materials and Engineering* 299.9 (2014), pp. 1052–1061. DOI: [10.1002/mame.201300390](https://doi.org/10.1002/mame.201300390).
- [5] Kelu Liu et al. “Cost-effective synthesis and superior electrochemical performance of sodium vanadium fluorophosphate nanoparticles encapsulated in conductive graphene network as high-voltage cathode for sodium-ion batteries”. In: *Journal of Colloid and Interface Science* 532 (2018), pp. 426–432. DOI: [10.1016/j.jcis.2018.07.114](https://doi.org/10.1016/j.jcis.2018.07.114).
- [6] Renzhong Chen et al. “Facile fabrication of foldable electrospun polyacrylonitrile-based carbon nanofibers for flexible lithium-ion batteries”. In: *Journal of Materials Chemistry A* 5.25 (2017), pp. 12914–12921. DOI: [10.1039/c7ta02528a](https://doi.org/10.1039/c7ta02528a).

- [7] M. M. Coleman and R. J. Petcavich. “Fourier Transform Infrared Studies on the Thermal Degradation of Polyacrylonitrile.” In: *J Polym Sci Polym Phys Ed* 16.5 (1978), pp. 821–832. DOI: [10.1002/pol.1978.180160507](https://doi.org/10.1002/pol.1978.180160507).
- [8] M.S.A. Rahaman, A.F. Ismail, and A. Mustafa. “A review of heat treatment on polyacrylonitrile fiber”. In: *Polymer Degradation and Stability* 92.8 (Aug. 2007), pp. 1421–1432. DOI: [10.1016/j.polymdegradstab.2007.03.023](https://doi.org/10.1016/j.polymdegradstab.2007.03.023).
- [9] Biao Zhang et al. “Correlation Between Atomic Structure and Electrochemical Performance of Anodes Made from Electrospun Carbon Nanofiber Films”. In: *Advanced Energy Materials* 4.7 (May 2014), p. 1301448. DOI: [10.1002/aenm.201301448](https://doi.org/10.1002/aenm.201301448).
- [10] Chan Kim et al. “Fabrication of electrospinning-derived carbon nanofiber webs for the anode material of lithium-ion secondary batteries”. In: *Advanced Functional Materials* 16.18 (2006), pp. 2393–2397. DOI: [10.1002/adfm.200500911](https://doi.org/10.1002/adfm.200500911).
- [11] Biao Zhang et al. “Recent advances in electrospun carbon nanofibers and their application in electrochemical energy storage”. In: *Progress in Materials Science* 76 (2016), pp. 319–380. DOI: [10.1016/j.pmatsci.2015.08.002](https://doi.org/10.1016/j.pmatsci.2015.08.002).
- [12] Tae-Jin Park et al. “Raman spectroscopic evaluation of polyacrylonitrile-based carbon nanofibers prepared by electrospinning”. In: *Journal of Raman Spectroscopy* 35.11 (2004), pp. 928–933. DOI: [10.1002/jrs.1233](https://doi.org/10.1002/jrs.1233).
- [13] P. Suresh Kumar et al. “Free-standing electrospun carbon nanofibres - A high performance anode material for lithium-ion batteries”. In: *Journal of Physics D: Applied Physics* 45.26 (2012). DOI: [10.1088/0022-3727/45/26/265302](https://doi.org/10.1088/0022-3727/45/26/265302).
- [14] Xinhua Liu et al. “Flexible all-fiber electrospun supercapacitor”. In: *Journal of Power Sources* 384.November 2017 (2018), pp. 264–269. DOI: [10.1016/j.jpowsour.2018.02.081](https://doi.org/10.1016/j.jpowsour.2018.02.081).
- [15] Myeong Jun Song et al. “Self-standing, binder-free electrospun Co₃O₄/carbon nanofiber composites for non-aqueous Li-air batteries”. In: *Electrochimica Acta* 182 (2015), pp. 289–296. DOI: [10.1016/j.electacta.2015.09.100](https://doi.org/10.1016/j.electacta.2015.09.100).
- [16] Jiangling Li et al. “Carbon nanowalls grown by microwave plasma enhanced chemical vapor deposition during the carbonization of polyacrylonitrile fibers”. In: *Journal of Applied Physics* 113.2 (2013). DOI: [10.1063/1.4774218](https://doi.org/10.1063/1.4774218).
- [17] Xiaoping Zhou et al. “Supercapacitors based on hybrid carbon nanofibers containing multiwalled carbon nanotubes”. In: *Journal of Materials Chemistry* 19.18 (2009), p. 2810. DOI: [10.1039/b820170f](https://doi.org/10.1039/b820170f).
- [18] Katsuya Sode et al. “Carbon nanofibers prepared from electrospun polyimide, polysulfone and polyacrylonitrile nanofibers by ion-beam irradiation”. In: *Polymer Journal* 45.12 (2013), pp. 1210–1215. DOI: [10.1038/pj.2013.56](https://doi.org/10.1038/pj.2013.56).
- [19] Ai Fu Che et al. “Fabrication of free-standing electrospun carbon nanofibers as efficient electrode materials for bioelectrocatalysis”. In: *New Journal of Chemistry* 35.12 (2011), pp. 2848–2853. DOI: [10.1039/c1nj20651f](https://doi.org/10.1039/c1nj20651f).

Chapter 4

Conclusions and Outlook

The field of sodium-ion batteries represents a hot topic for research groups. With more than 7000 papers published in the last five years [1], plenty of cathode and anode materials have been studied, synthesized and characterized, as well as optimal electrolyte compositions and concentrations have been developed. Thanks to the widely abundant precursors and the low environmental impact, SIB are the most promising alternative to LIB in those applications that require no outstanding energy and power densities. For consumable electronics, LIB will still be the mainstream choice, as they offer the best volumetric and gravimetric energy densities, a key design parameter for laptops and smartphones. However, SIB could prove to be fundamental in fostering energy transition by serving as stationary energy storage for renewables sources. In this case, battery weight and volume is a second order issue if compared to the benefits of having a low cost storage system.

This being said, one may wonder why SIB are still mostly investigated at laboratory level. Undoubtedly, the efforts made by researchers worldwide can only merge together if common protocols and clear benchmark values are defined [2]. Then, an eye has to be kept in implementing real SIB systems, where materials performances can be evaluated "in vivo" and not only in half cells, "in vitro", systems.

From an engineering perspective, the idea of introducing some kind of "technology booster" to enhance the properties of materials that would otherwise be always secondary to lithium compounds, is thrilling and can help bridging the gap between research and industry.

With this mindset, a scalable and low cost process flow to fabricate CNF electrode supports was experimentally assessed and characterized. Carbon nanofibers can be obtained by electrospinning starting from PAN solution and exploiting successive thermal treatments. Spinning and stabilization parameters were studied in order to obtain reproducible mats with different thicknesses. These were carbonized and then loaded with NVP to be used as cathodes in a sodium half cell, as described in [3]. Fundamentals features and advantages of such electrospun supports are:

- scalability and cost effectiveness of the electrospinning process;
- controllability of mat thickness by acting on spinning parameters;
- interconnected porosity of the mat, both before and after carbonization;

Lastly, future work to be carried out on the first process can be summarized as follows:

- optimization of electrospinning conditions is needed, in particular humidity and temperature, in order to have mats produced with high process efficiency *i.e.* thick mats in a short time;
- systematic study should be performed on mats thickness and its growth process in relation to spinning parameters;

- investigation of different setups, for example multi-needle spinning and different collector geometry to obtain different porosity grades;
- possibility of having only one process substrate would be convenient to scale up the process. For instance steel could be used as collector and support during stabilization and carbonization. If mat adhesion on the substrate is good enough, the layered structure substrate-mat could be directly exploited in the cell;
- further optimization of stabilization must be performed, in particular with respect to mechanical properties, in order to obtain mats easy to handle and to process further;
- optimization of carbonization procedure, in order to obtain CNF with higher electrical conductivity ($> 10 \text{ S cm}^{-1}$)

References

- [1] Clarivate. *Sodium Ion Battery Publications Statistics*. 2019.
- [2] Yuliang Cao et al. “Bridging the academic and industrial metrics for next-generation practical batteries”. In: *Nature Nanotechnology* 14.3 (2019), pp. 200–207. DOI: [10.1038/s41565-019-0371-8](https://doi.org/10.1038/s41565-019-0371-8).
- [3] Jacopo Celè. “Study of the Effect of Carbon Nanofibers Electrodes Morphology on Sodium-ion Cells Electrochemical Performances”. MA thesis. Politecnico di Torino, 2019.

Chapter 5

APPENDIX

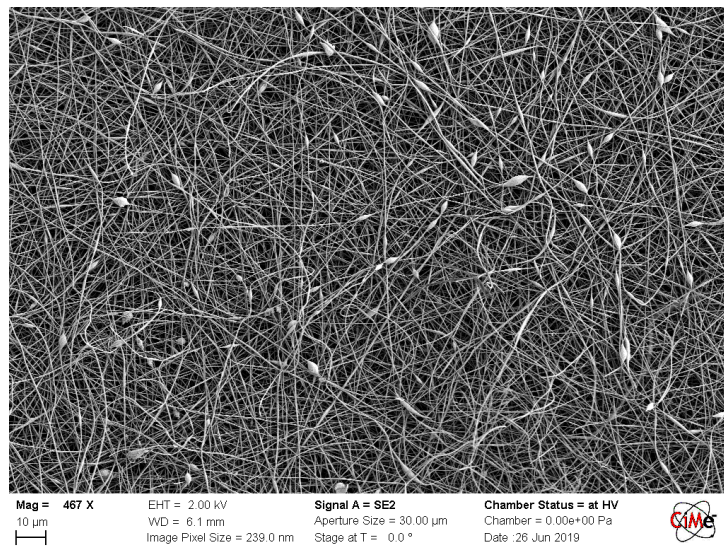


Figure 5.1: Mat surface morphology. Some beads are present along the fiber axis.

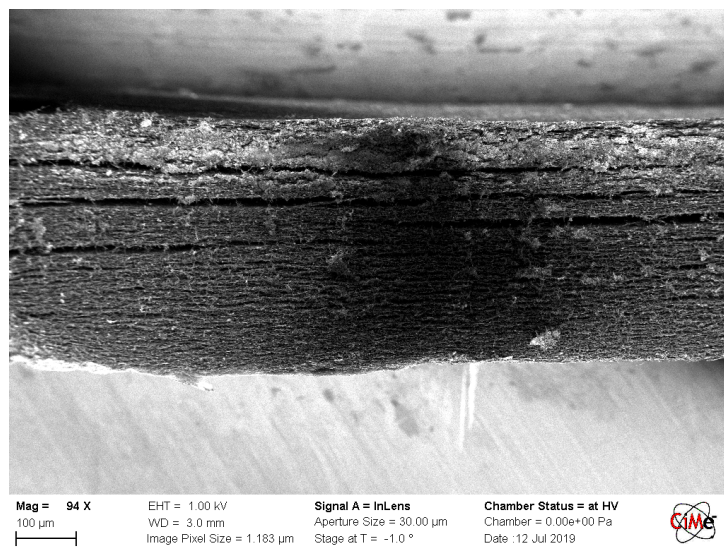


Figure 5.2: Mat after NVP loading, visible on the mat surface. This procedure was not optimal and NVP was not uniformly distributed in the mat.

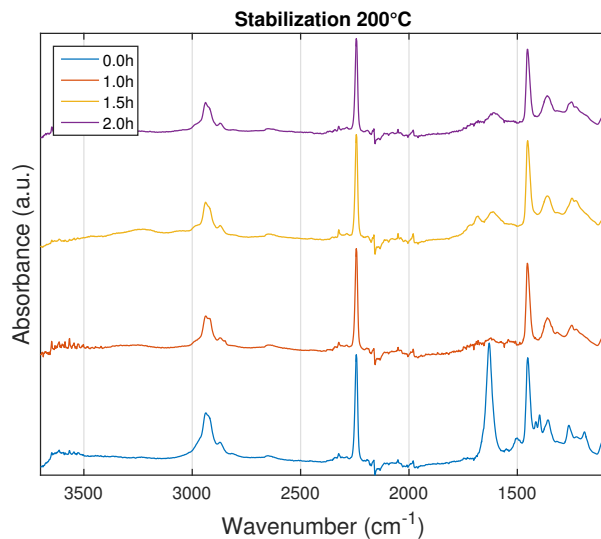


Figure 5.3: FTIR of 200 °C stabilization.

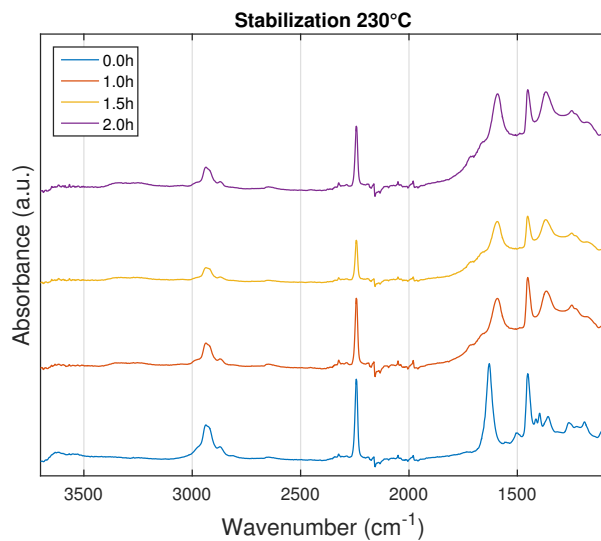


Figure 5.4: FTIR of 230 °C stabilization.

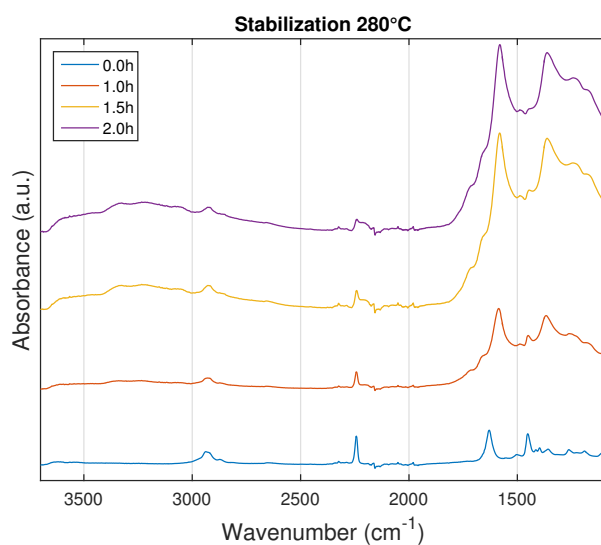


Figure 5.5: FTIR of 280 °C stabilization.

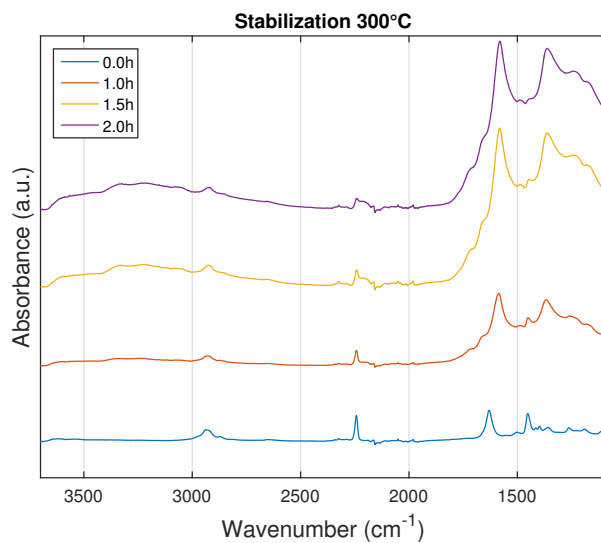


Figure 5.6: FTIR of 300 °C stabilization.

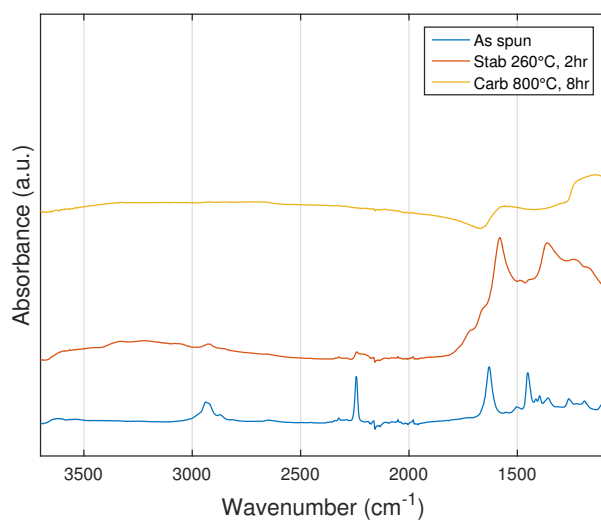


Figure 5.7: FTIR comparison of as spun, stabilized and post carbonization fibers.

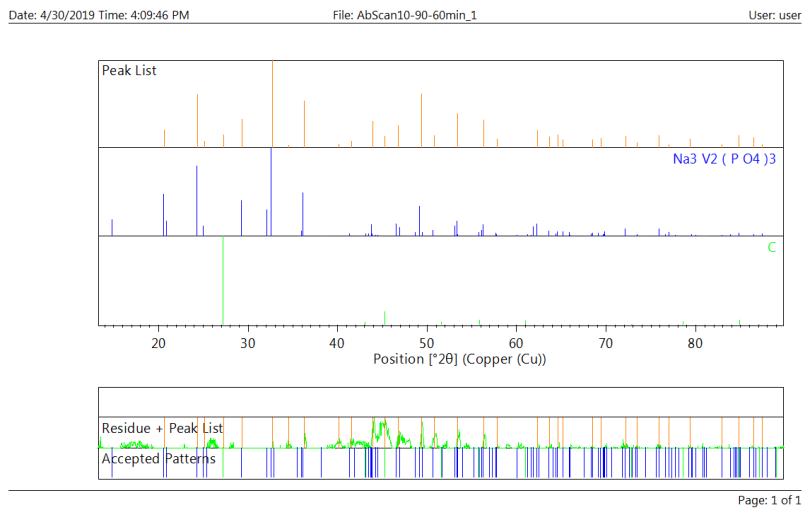


Figure 5.8: HighScore Peak match of powder XRD on CNF/NVP.

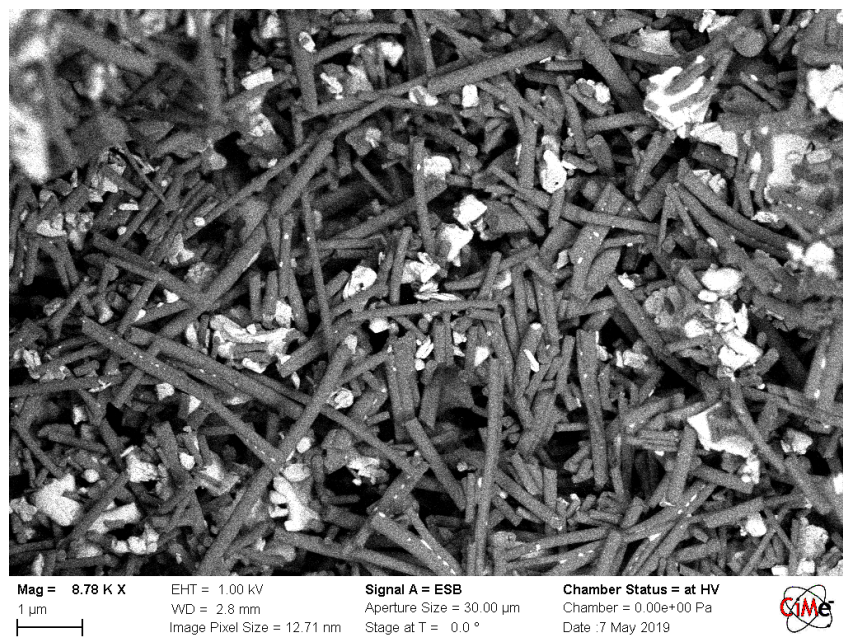


Figure 5.9: SEM on CNF/NVP powder used for XR.D

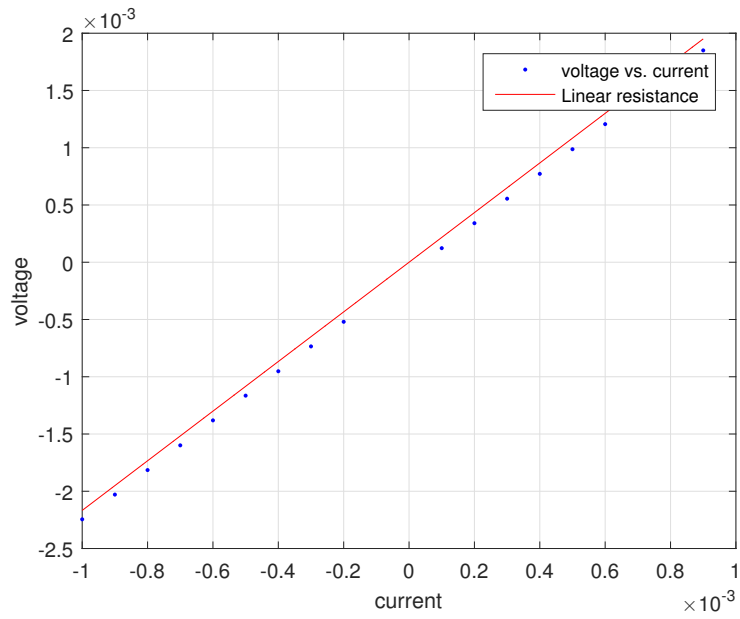


Figure 5.10: Fit of the I versus V values of transversal conductivity measurement.

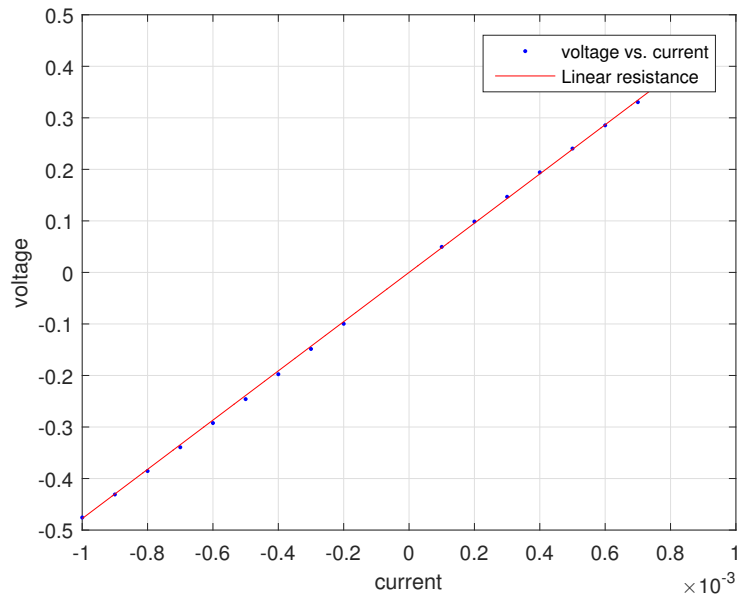


Figure 5.11: Fit of the I versus V values of longitudinal conductivity measurement.

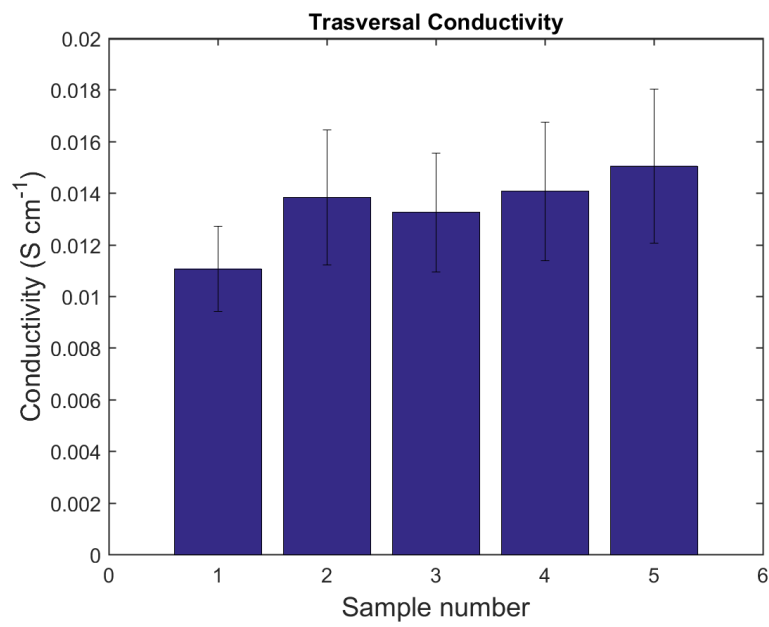


Figure 5.12: Comparison of transversal conductivity values obtained from 5 samples.